frontiers | Frontiers in Nuclear Engineering

TYPE Original Research
PUBLISHED 27 March 2023
DOI 10.3389/fnuen.2023.1142823

OPEN ACCESS

EDITED BY
Bernd Grambow,
UMR6457 Laboratoire de Physique Subatomique et des Technologies Associées (SUBATECH), France

REVIEWED BY
Vladimir Petrov,
Lomonosov Moscow State University, Russia
Sarah Saslow,
Pacific Northwest National Laboratory (DOE), United States
Tomo Suzuki-Muresan,
UMR6457 Laboratoire de Physique Subatomique et des Technologies Associées (SUBATECH), France

*CORRESPONDENCE
Ibrahim Maamoun,
maamoun.ibrahim@jaea.go.jp

SPECIALTY SECTION
This article was submitted to Radioactive Waste Management, a section of the journal Frontiers in Nuclear Engineering

RECEIVED 12 January 2023
ACCEPTED 17 March 2023
PUBLISHED 27 March 2023

CITATION
Maamoun I, Tokunaga K, Dohi T, Kanno F, Falyouna O, Eljamal O and Tanaka K (2023), Improved immobilization of Re(VII) from aqueous solutions *via* bimetallic Ni/Fe^0 nanoparticles: Implications towards Tc(VII) removal. *Front. Nucl. Eng.* 2:1142823. doi: 10.3389/fnuen.2023.1142823

Improved immobilization of Re(VII) from aqueous solutions *via* bimetallic Ni/Fe^0 nanoparticles: Implications towards Tc(VII) removal

Ibrahim Maamoun[1]*, Kohei Tokunaga[1,2], Terumi Dohi[3], Futoshi Kanno[3], Omar Falyouna[4], Osama Eljamal[4] and Kazuya Tanaka[1]

[1]Advanced Science Research Center, Japan Atomic Energy Agency, Tokai, Ibaraki, Japan, [2]Ningyo-toge Environmental Engineering Center, Japan Atomic Energy Agency, Tomata, Okayama, Japan, [3]Sector of Fukushima Research and Development, Japan Atomic Energy Agency, Fukushima, Japan, [4]Department of Earth System Science and Technology, Water and Environmental Engineering Laboratory, Interdisciplinary Graduate School of Engineering Sciences, Kyushu University, Fukuoka, Japan

Introduction: In this work, bimetallic nickel/iron nanoparticles (Ni/Fe^0) were prepared to enhance rhenium (Re(VII)) immobilization from aqueous solutions, as the surrogate of technetium (Tc(VII)).

Methods: Two synthesis approaches of Ni/Fe^0, pre-, and post-nucleation, were investigated towards Re(VII) removal. Different characterization techniques were considered to elucidate the physicochemical features of the fresh and reacted materials, such as scanning transmission electron microscopy-energy dispersive X-ray spectroscopy (STEM-EDX), X-ray diffraction (XRD), and X-ray absorption near edge spectroscopy (XANES). The influence of several reaction parameters on Re(VII) removal was investigated, including Ni/Fe^0 ratio, dosage, initial pH, temperature, and initial concentration.

Results and discussion: Results showed a promising potential of Ni/Fe^0, either pre- or post-nucleation synthesized, in Re(VII) removal, especially at the early stage of the reaction, where Ni/Fe^0: 0.4 yielded almost full removal efficiency of initial 15.0 μM-Re(VII) within the first 10 min of reaction. Even at low Ni/Fe^0 dosages, such as 0.25 and 0.5 g/L, reasonable removal efficiency was achieved after 2 h reaction time of ~73% and ~98%, respectively. Unlike acidic/neutral pH, alkaline conditions were not favorable for Re(VII) removal by Ni/Fe^0 owing to the delayed aqueous corrosion of Fe^0-core resulting in insufficiency of electrons available for Re(VII) reduction. The reductive abilities were confirmed by XANES, revealing Re(VII) reduction to Re(IV)/(III) by the released electrons from Fe^0-core in both Fe^0 and Ni/Fe^0 materials. Pseudo-first- and second-order kinetic models were suitable to describe Re(VII) removal by Ni/Fe^0, implying physical and/or chemical processes were involved. Zeta potential measurements depicted the point of zero charge (pH$_{PZC}$) of Fe^0 and Ni/Fe^0 to be 8.24 and 7.63, respectively, suggesting the involvement of electrostatic sorption of ReO_{4-} on the positively charged surface of Ni/Fe^0. The occurrence of multi- and mono-layer sorption within Re(VII) removal process was implicated, following Freundlich and Sips isotherm models. The presence of Ni^0/NiO on Fe^0-surface resulted in providing an efficient electron-transfer medium that facilitated Re(VII)

reduction, leading to impressive kinetic rates. Overall, our study provided valuable insights into the use of Ni/Fe^0 for Re(VII) removal from water and offered guidance for future research in such an aspect towards the pilot-scale applications of Tc(VII) removal from nuclear wastewater.

KEYWORDS

bimetallic iron nanoparticles, rhenium (VII), reduction, characterization, removal mechanism, kinetics

1 Introduction

The rapid development of nuclear power technologies has led to increased water contamination around the world. Nuclear industries produce large amounts of wastewater as a byproduct of the generation of nuclear energy, containing a variety of harmful contaminants, including radionuclides, heavy metals, and other chemicals (Sakaguchi et al., 2012; Tanaka et al., 2012). Nuclear power plants represent the major source of radioactive contamination in many countries, including France, Germany, Japan, the United Kingdom, and the United States, with more than 90% of the radioactive contaminants in the discharged wastewater from nuclear power and fuel reprocessing plants (Chung et al., 2011; Sheng et al., 2016). Correspondingly, the continued growth of the nuclear power industry is likely to result in even more water contamination in the future. Technetium-99 (^{99}Tc) is one of the long-lived radionuclides (half-life: ~2.13×10^5 years), which represents the main fission products of uranium-238 (^{238}U) (Burton-Pye et al., 2011; Fan et al., 2013). ^{99}Tc commonly occurs in the heptavalent (Tc(VII)) anionic form of pertechnetate (TcO_4^-), which is highly mobile and soluble (Tanaka et al., 2019b). Tc(VII) enters water sources through contamination from industrial processes, such as the reprocessing of nuclear fuels. In large enough quantities, Tc(VII) can be harmful to human health, as it causes toxic effects if ingested and damage kidneys and other organs when exposed to its high levels (Cothern and Lappenbusch, 1985; Fu et al., 2020). Additionally, Tc-related issues and challenges are persistent within various nuclear industry applications. For instance, one of the long-term technical challenges of Tc separation is the volatility of its compounds within the vitrification of low activity nuclear waste. Tc(VII) is significantly volatile at the high typical vitrification temperatures (1,100—1,200°C), unlike it reduced form (Tc(IV)) which is less volatile under such conditions (Lukens et al., 2007). Such challenge is faced during the treatment process of low activity waste stream *via* Tc combination with borosilicate glass, where volatile Tc(VII) is recovered in the off-gas condensate solution within the treatment system (Boglaienko et al., 2019). Meanwhile, Tc remains a major environmental problem at nuclear reprocessing plants, where Tc-loaded liquid waste is released into the subsurface environment. The high abundance of Tc in such liquid waste suggests the challenge of aqueous immobilization of the highly mobile Tc(VII). It is critical for Tc(VII) in aqueous waste streams to be immobilized into a stable form towards waste disposal with less environmental contamination risks. Hence, the rapid and efficient Tc(VII) removal from radioactive water has emerged as a challenging issue. Correspondingly, the reduction separation of the highly mobile and soluble Tc(VII) to Tc(IV), which is much less mobile and soluble in the environment, by electron-donor materials would be significantly beneficial with regard to the abovementioned challenges.

Zero-valent iron nanoparticles (Fe^0) have been widely utilized as an efficient reactive material towards reducible contaminants owing to the suitable redox potential and the unique core-shell structure. Several removal mechanisms can be involved within the reaction of Fe^0 with most of the soluble contaminants, including reduction by the released electron from the iron core (electron donor), adsorption on the formed passivation iron oxy/hydroxide shell (high-capacity adsorbent), and possible co-precipitation of contaminants species with the released iron oxides (precipitation facilitator) (Tosco et al., 2014; Mukherjee et al., 2016). Nevertheless, several modification techniques have been suggested to overcome Fe^0 drawbacks in real water treatment applications (e.g., aggregation, poor aqueous suspension, and low mobility), including stabilization (Eljamal et al., 2020), supporting (Idham et al., 2022; Islam et al., 2023), coating (Maamoun et al., 2022b, 2023b). In spite of the efficacy of these modification techniques in solving Fe^0 issues, they are not favorable for reducible contaminants, whose removal process requires rapid release of electrons from the iron core and highly reactive surface of the particles. Using polymer stabilizers or non-magnetic coating materials shall improve the anti-aggregation effect of Fe^0 nanoparticles, yet the iron-core consumption can be delayed causing a progressive reduction of the contaminants, which has been previously proven towards the reducible nitrate (NO_3^-) (Eljamal et al., 2020; Maamoun et al., 2020). The non-magnetic coating of magnesium hydroxide, with moderate water-solubility, exhibited efficient preservation of the Fe^0-core from the rapid consumption, preventing the formation of the passivation film on the surface of the nanoparticles; confirmed by the low-release profiles of Fe(II/III) (Maamoun et al., 2020, 2022b). Meanwhile, despite the anti-aggregation effect, supporting Fe^0 nanoparticles on high-surface area supporting materials is not as efficient as the coating modification techniques in suppressing the surface passivation. Hence, doping the surface of Fe^0 with another metal (e.g., copper (Cu), palladium (Pd), platinum (Pt), silver (Ag), nickel (Ni), *etc.*) yields bimetallic nanoparticles with a remarkably reactive surface, higher catalytic properties, and improved removal capabilities towards reducible contaminants (Rivero-Huguet and Marshall, 2009). Different studies reported the superiority of Pd and Ni, as the doped-metal, to most other metals, represented by better removal of reducible contaminants, such as nitrate, hexavalent chromium, trichloroethylene, and chlorinated organic compounds (Yang et al., 2008; Rivero-Huguet and Marshall, 2009; Zhang et al., 2010; Liu et al., 2022; Venkateshaiah et al., 2022). Nevertheless, using Ni in bimetallic Fe^0 may have advantageous features, including the cost-efficiency (compared to the high-cost Pd), the catalytic activity of Ni, the ability to act as an electron transfer medium to overcome the self-inhibition in electron transfer, and the high specific surface area of Ni/Fe^0 material that yields more active sites (Liu et al., 2022). The potential of metal doping in enhancing the kinetic rate of iron-based materials

towards ^{99}Tc was recently explored. Lee et al. investigated the effect of modifying magnetite with Ni, Zn, and Co. metal dopants on ^{99}Tc incorporation and retention, where the highest retention rates were recorded for Co.; by increasing the overall reducing capacity of the spinel material (Lee et al., 2016, 2020). Nevertheless, it is still worthy to investigate the effect of metal doping on the chemically synthesized Fe^0 nanoparticles, as a material with high reactivity, and the corresponding influence on Tc(VII) reduction rate.

$$ReO_4^- + 4H^+ + 3e^- \rightarrow ReO_2 + 2H_2O \quad (E^0 = -0.548\,V) \quad (1)$$

$$TcO_4^- + 4H^+ + 3e^- \rightarrow TcO_2 + 2H_2O \quad (E^0 = -0.361\,V) \quad (2)$$

Rhenium (Re) is considered the common chemical analogue for Tc owing to their similar physiochemical features. Both Re and Tc share the same stable VII oxidation state of perrhenate (ReO_4^-) and pertechnetate (TcO_4^-), respectively (Li et al., 2016). Furthermore, both ReO_4^- and TcO_4^- can be reduced to IV oxidation state *via* electron-donor materials, with a standard redox potential (E^0) of −0.548 V and −0.361 V, respectively (Maset et al., 2006; Liu et al., 2013; Wu et al., 2014). Such a difference in reduction potential reflects that Tc(VII) is easier to be reduced than Re(VII) which requires more drastic reduction conditions, which has been previously proven (Maset et al., 2006; Dolor et al., 2009). Hence, to ease the experimental work and avoid radioactivity-related complications, Re(VII) was considered the target contaminant in this work as Tc(VII) analogue. Nevertheless, several reports focused on studying their chemical differences under different redox conditions, which influences the applicability of Re as a Tc surrogate (Lukens et al., 2007; Buechele et al., 2010; Kim and Kruger, 2018). For instance, dissimilarities were observed in the speciation and volatility of Re and Tc species, where Re(IV) disproportionation at high temperatures caused its instability, unlike the Tc(IV). Such observations implied the crucial role of controlling Tc volatility within the real applications of nuclear waste vitrification (Lukens et al., 2007). Thus, Re can be a good Tc surrogate under oxidizing conditions, while any slight change towards the reducing conditions may limit its applicability (Lukens et al., 2007; Kim and Kruger, 2018). Hence, it is crucial to study the potential of electron-donor materials for the reduction of both Re(VII) and Tc(VII) at different redox conditions to predict their behaviors in the real complex systems.

In this regard, several reported studies investigated the use of Fe^0-based materials for the reductive immobilization of Tc(VII) and/or Re(VII). Lingxiao et al. used Fe^0 nanoparticles supported on D001 resin for the removal of Re(VII) from water within batch and column experiments (Fu et al., 2020). In spite of the well-known high reactivity of experimentally synthesized Fe^0 *via* chemical reduction method, just ~80% Re(VII) removal efficiency was achieved after 24 h reaction time considering 10 mg/L initial Re(VII) concentration and 10 g/L D001- Fe^0 (Fu et al., 2020). A relatively slow kinetic rate was observed, which could be infeasible considering the high Fe^0-based material dosage and the acidic pH conditions. In another study, porous and granular iron (pFe and gFe) were used for Re(VII) removal from artificial groundwater, where high dosages of pFe and gFe (up to 10 g/L) were required to remove ~97% and 12%, respectively, of 0.06 mM initial Re(VII) concentration at pH 6.7 (Li et al., 2019). Li et al. studied the reductive immobilization of Re(VII) by graphene-modified Fe^0 using a plasma technique, where a pH-dependent removal process was determined (Li et al., 2016). At neutral pH, rGO-Fe^0 achieved an equilibrium Re(VII) removal efficiency of ~15%, with a slow kinetic rate which needed ~50 min to be reached (0.1 g/L dosage and 20 mg/L initial Re(VII) concentration) (Li et al., 2016). Contrarily, pH 3.8 exhibited ~65% removal efficiency after 1-h reaction time (Li et al., 2016). Hence, it can be implicated that a higher kinetic rate is one of the challenges in Re(VII) removal process that should be addressed. With regard to Tc(VII) reduction by Fe^0-based materials, Emerson et al. used commercial Fe^0, with an average particle size of 75 μm, for Tc(VII) reduction to Tc(IV) at initial neutral pH and 0.08 M NaCl. Fe^0 dosage of 0.5 g/L achieved >99% removal efficiency of initial Tc(VII) concentration of 500 μg/L (5.0 μM); while aging time of Fe^0 was a crucial factor (Emerson et al., 2020). In another study, the manufacturing method of commercial Fe^0 had a significant effect on its reductive separation of Tc(VII) from aqueous waste streams, where electrolytic method showed the best removal performance (Boglaienko et al., 2019). As formerly mentioned, using supporting materials (with high specific surface area) or polymer/organic stabilizers to modify Fe^0 can overcome its aqueous issues. The discrete distribution of Fe^0 nanoparticles on the supporting material or the anti-aggregation effect of the stabilizer may provide higher specific surface area of the particles and thereby more available binding sites. Darab et al. studied supported Fe^0 on different inorganic supporting materials, where nanocrystalline zirconia-supported Fe^0 and silica-supported Fe^0 could efficiently remove TcO_4^- from simulated nuclear waste streams at highly alkaline and near-neutral conditions, respectively (Darab et al., 2007). Meanwhile, using a water-soluble starch stabilizer for Fe^0 nanoparticles enhanced the anti-aggregation effect as long with exhibiting high Re(VII) reduction rate constants, especially at high reaction temperatures (0.428 1/hr at 45°C) (Ding et al., 2013).

Despite the adequate number of reported studies on Tc(VII) and/or Re(VII) removal by Fe^0-based materials, there is a gap in the literature on using bimetallic Fe^0 in this regard, especially Ni/Fe^0 material. Hence, the aim of this work is to utilize bimetallic nickel/iron nanoparticles (Ni/Fe^0) in enhancing the immobilization of rhenium Re(VII) from aqueous solutions, as the surrogate of Tc(VII). The specific objectives of this paper are: (1) Investigating two synthesis approaches of Ni/Fe^0, pre-, and post-nucleation, towards Re(VII) removal; (2) detailed characterization of fresh and reacted Fe^0 and Ni/Fe^0, considering scanning transmission electron microscopy-energy dispersive X-ray spectroscopy (STEM-EDX), X-ray diffraction (XRD), and X-ray absorption near edge structure (XANES); (3) determination of the influence of various reaction parameters on removal efficiency, including Ni/Fe^0 ratio, dosage, initial pH, reaction temperature, and initial Re(VII) concentration; (4) interpreting experimental removal data *via* kinetic, isotherm, and thermodynamic models; (5) revealing the removal pathways of Re(VII) by Ni/Fe^0 and evaluating the potential limitations and challenges of this technology.

2 Materials and methods

2.1 Chemicals

Ferric chloride hexahydrate ($FeCl_3.6H_2O$, purity >99.0%, FUJIFILM Wako Co., Japan), and sodium borohydride ($NaBH_4$,

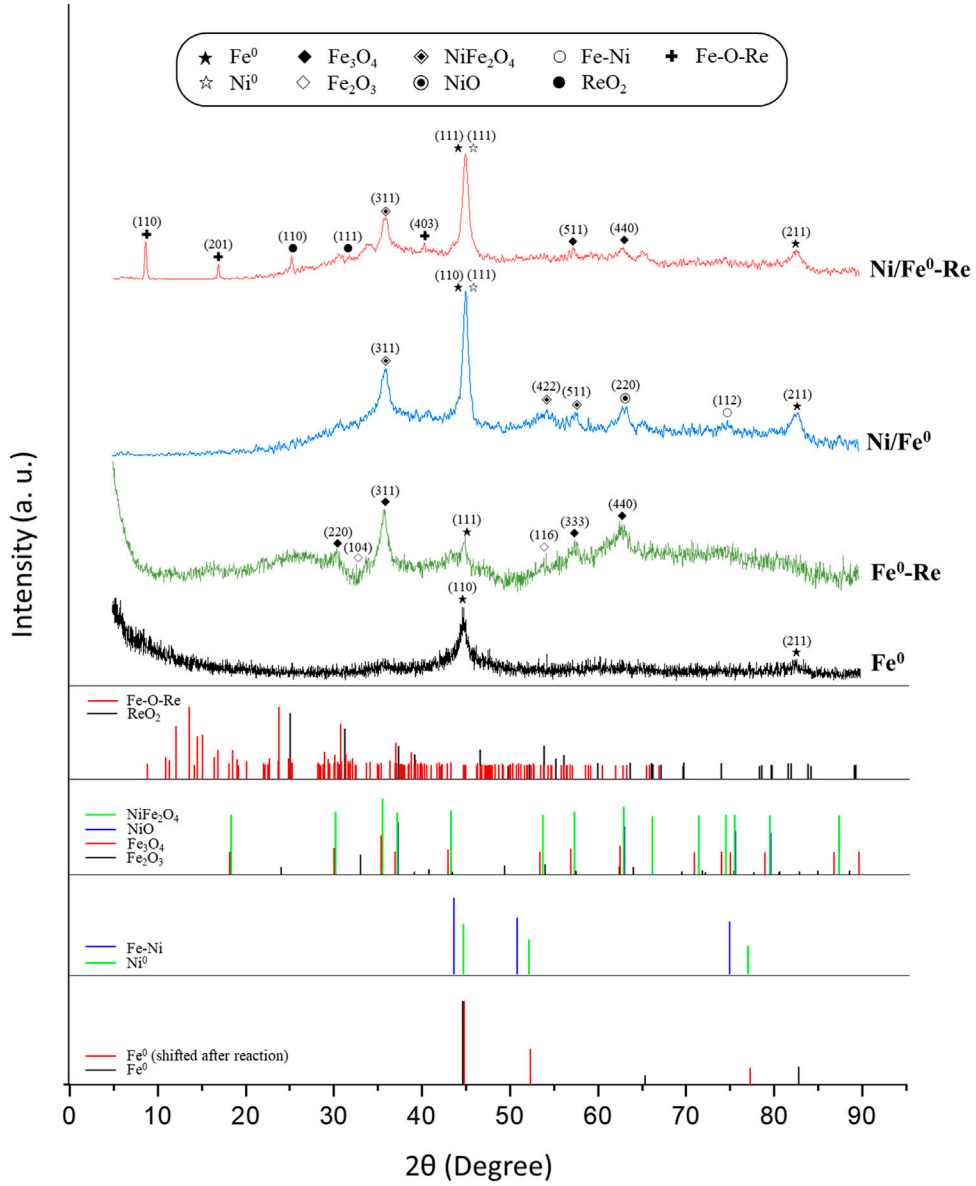

FIGURE 1
XRD patterns of fresh and spent Fe^0 and Ni/Fe^0 (reaction conditions: ~100 μM initial Re(VII) concentration, and 5.0 ± 0.2 initial pH).

purity >95.0%, Tokyo Chemical Industry Co. (TCI), Japan) were used for the synthesis of Fe^0. Nickel chloride hexahydrate ($NiCl_2.6H_2O$, purity >98.0%, FUJIFILM Wako Co., Japan) was used as Ni^{2+} source in the preparation of Ni/Fe^0. Ammonium perrhenate (NH_4ReO_4, purity >99.0%, Sigma Aldrich Inc, United States) was considered for the preparation of Re(VII) stock solutions. Sodium hydroxide (NaOH, FUJIFILM Wako Co., Japan), and nitric acid (HNO_3, FUJIFILM Wako Co., Japan) were used for pH adjustment. Sodium chloride (NaCl, purity >99.5%, FUJIFILM Wako Co., Japan), sodium nitrate ($NaNO_3$, purity >99.0%, Kanto Chemical Co. Inc, Japan), and sodium sulfate (Na_2SO_4, purity >99.0%, FUJIFILM Wako Co., Japan) were used in the co-existing ions experiments. Anthrarufin or 1,5-dihydroxyanthraquinone ($C_{14}H_8O_4$, Tokyo Chemical Industry Co. (TCI), Japan) was used to study the effect of Fe(II)-chelating agent on Re(VII) removal. Ethanol (C_2H_5OH, purity >99.5%, FUJIFILM Wako Co., Japan) was used for washing the freshly synthesized materials. Ultrapure water (Millipore Direct-Q® 3UV Water Purification System, Millipore Sigma Co. United States) was considered for preparing all solutions. All solutions were purged with argon (Ar) gas before being used in synthesis or immobilization experiments.

2.2 Fe^0 synthesis

Fe^0 was experimentally prepared using the chemical reduction of ferric precursor by borohydride reductant within the aqueous phase.

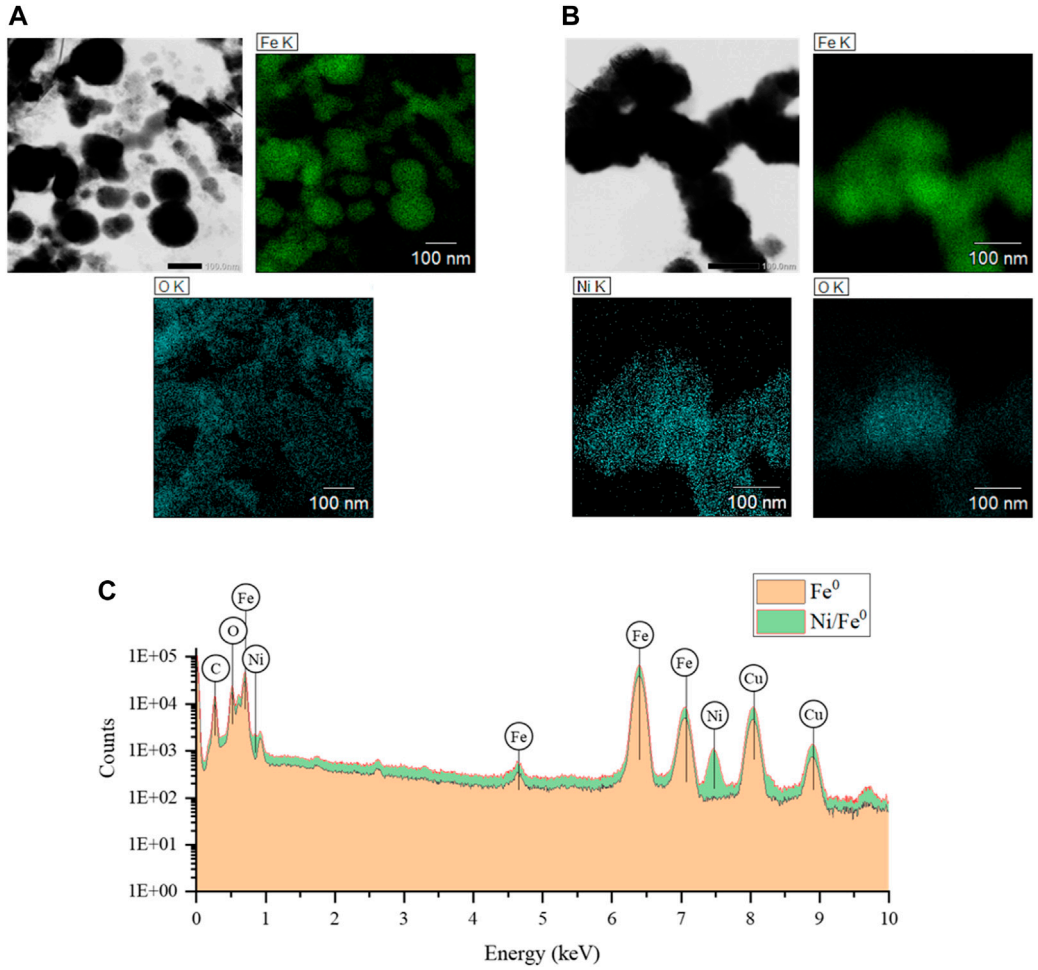

FIGURE 2
STEM imaging and EDS elemental mapping of freshly synthesized Fe^0 **(A)**, Ni/Fe^0 **(B)**, and corresponding spectra **(C)** (reaction conditions: ~15.0 μM initial Re(VII) concentration, and 5.0 ± 0.2 initial pH).

Synthesis conditions were typical to the previously conducted optimization of Fe^0 synthesis (Maamoun et al., 2023a). Briefly, the reductant solution was added incrementally to the precursor solution considering a precursor/reductant mass ratio of 2.27, and mechanically mixed at 300 RPM. The synthesis was conducted in a water bath at 30°C ± 1.0 and under Ar gas pruning to provide an anaerobic environment. After agitating time of 5 min, the black Fe^0 precipitates were collected *via* vacuum filtration (0.45 μm membrane filter, Advantec Co., Japan) and washed several times with ethanol. The freshly synthesized Fe^0 was immediately used for Re(VII) immobilization experiments without any pre-storage.

2.3 Ni/Fe^0 synthesis

Two different approaches were considered for the preparation of Ni/Fe^0, considering Fe-nucleation as the reference. The first approach, pre-nucleation, involved adding Ni^{2+} precursor into the ferric solution before being reduced by the borohydride reductant. While the post-nucleation approach considered the addition of the freshly synthesized Fe^0 to Ni^{2+} solution. 30 min mixing under Ar gas purging was utilized in both pre- and post-nucleation approaches. Nevertheless, in the case of post-nucleation approach, Fe^0 suspension was ultrasonicated for 20 min before the mixing process before being introduced to the Ni^{2+} solution. Different Ni/Fe^0 mass ratios were considered in both synthesis approaches, including Ni/Fe^0 (wt/wt): 0.05, 0.1, 0.2, and 0.4. The synthesized Ni/Fe^0 was filtrated following the formerly mentioned procedure and used immediately in Re(VII) immobilization experiments. It is worth mentioning that Ar gas was used during the whole filtration process of Fe^0 and/or Ni/Fe^0, to avoid the oxidation of the reactive materials before the reaction with Re(VII).

2.4 Materials characterization

Different characterization techniques were considered to investigate the physicochemical properties of the fresh and spent materials. X-ray diffraction (XRD, Rigaku SmartLab II, Rigaku Co. Ltd., Japan) was considered to identify the crystal structure, phases,

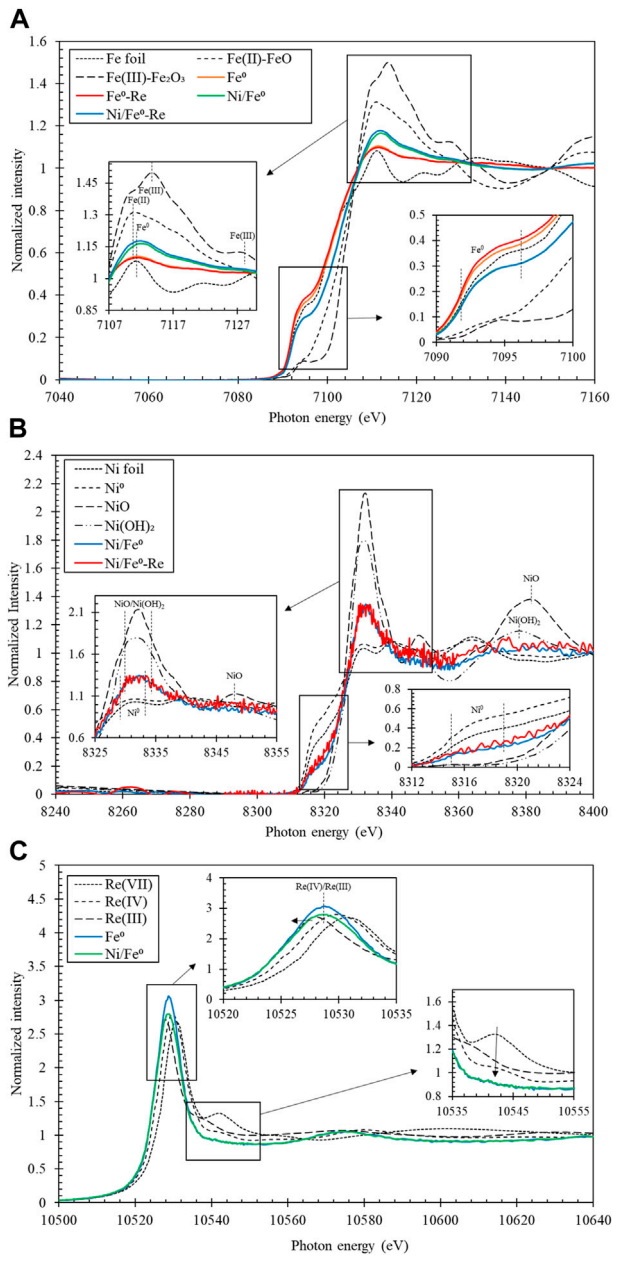

FIGURE 3
XANES spectra of fresh and spent Fe^0 and Ni/Fe^0: Fe K-edge **(A)**, Ni K-edge **(B)**, and Re L_{III}-edge **(C)**.

and composition of the materials; using Cu Kα radiation (40 mA current, 40 kV voltage, 3°/min scanning rate, 0.01° scanning step, and 5°—90° scanning range). SmartLab Studio II, Rigaku Co. Ltd. was used as the processing software, and integrated X-ray powder diffraction software (PDXL ver. 2.8.4, Rigaku Co. Ltd.) was used for XRD patterns analysis. Powder samples were characterized using high quality glass XRD sample holder (>99.9% (4N) purity silica, >80% transmittance). Scanning transmission electron microscopy-energy dispersive X-ray spectroscopy (STEM-EDS, JEM-2800, JEOL Co., Japan) was used to determine the morphological features and the elemental composition of the materials by analyzing the characteristic X-ray energy, considering 200 kV voltage. Powder samples were dispersed in ethanol under ultrasonication before being introduced to TEM grid (Cu150). After room-temperature drying, sample-loaded grid was set in the TEM holder, then cleaned using Plasma Cleaner (PIE Scientific) for removing hydrocarbon contamination before the analysis. Acquisition time of EDS mapping was 250 s (1 frame/10 s) and dwell time was 152 μsec (10 s/(map resolution 256 × 256 pixels)). Further SEM-EDS measurements were conducted for spent Fe^0 and Ni/Fe^0 (loaded with high Re concentration (~100 μM)), using JSM-IT700HR InTouchScope SEM (JEOL United States, Inco, United States). The measurements conditions involved 5.0 kV accelerated voltage, high vacuum mode, and 1647 CPS count rate. XANES measurements of Re L_{III}-edge, Fe K-edge, and Ni K-edge (fluorescence/transmission modes, beamline 12C) were conducted at the Photon Factory (KEK, Tsukuba, Japan) for the determination of the nature of fresh and spent materials as well as the oxidation states of the loaded Re species on the spent Fe^0 and Ni/Fe^0. For energy calibration, Fe-foil and Ni-foil were used for Fe and Ni K-edges, respectively. NH_4ReO_4 was used for calibration at Re L_{III}-edge. Empirically, it was confirmed that energy position did not shift by replicate measurements of the same standard sample. Standard materials for XANES measurements were by Fe K-edge (Fe foil [calib.], Fe^0 [synthesized metallic powder], Fe(II) [FeO], and Fe(III) [Fe_2O_3]), Ni K-edge (Ni foil [calib.], Ni [metallic powder], Ni(II) [NiO], and Ni(II) [$Ni(OH)_2$]), and Re L_{III}-edge (Re(VII) [NH_4ReO_4 calib.], Re(IV) [ReO_2], and Re(III) [$K_3(ReCl_6)$]). For Fe and Ni K-edges (I_0) ion chamber for incident X-ray was filled with N_2 gas, while (I) ion chamber for transmitted X-ray was filled with N_2 (75%) + Ar (25%). For Re L_{III}-edge (I_0) ion chamber was filled with N_2 (85%) + Ar (15%) gas, while (I) ion chamber was filled with N_2 (75%) + Ar (25%). Step sizes were 2—5 eV, 0.25 eV, and 1—2 eV for pre-edge, XANES, and post-edge regions, respectively. Collection time was 0.5 s at each step for transmission mode, and 2—3 s for fluorescence mode. For the analysis of XANES spectra, REX2000 ver. 2.5.9 (Rigaku Co. Ltd.) was used.

2.5 Re(VII) immobilization

Batch experiments were conducted to evaluate the efficiency of Fe^0 and Ni/Fe^0 in Re(VII) removal from aqueous solutions. Several reaction parameters were investigated, in the exact following sequence, including Ni/Fe^0 (wt/wt) ratio (0.05, 0.1, 0.2, and 0.4), Ni/Fe^0 dosage (0.25, 0.5, 1.0, 1.5, and 2.0 g/L), initial pH (3.0, 5.0, 7.0, 9.0 and 12.0), reaction temperature (25, 35, 45, and 55°C), and initial Re(VII) concentration (0.25, 0.5, 1.0, 5.0, 15.0, 25.0, and 50.0 μM). The baseline conditions for the reaction parameters optimization were an initial Re(VII) concentration of 15.0 ± 0.62 μM initial Re(VII) concentration, 1.0 g/L dosage, initial pH of 5.0 ± 0.2, and reaction temperature of 25 ± 1.0°C. It is worth mentioning that the initial concentration range was decided considering Tc waste concentrations in real contaminated sites (e.g., DOE Savannah River Site (SRS)) to be relevant to remediation scenarios (Stallings et al., 2005; Li et al., 2019). The Water samples were periodically withdrawn over 120 min reaction time to be analyzed for Re(VII) concentration using an inductively coupled plasma mass spectrometer (ICP-MS, Agilent 7,500, Agilent, Santa Clara, CA, United States). Re(VII) removal efficiency and uptake capacity were calculated according to the following equations:

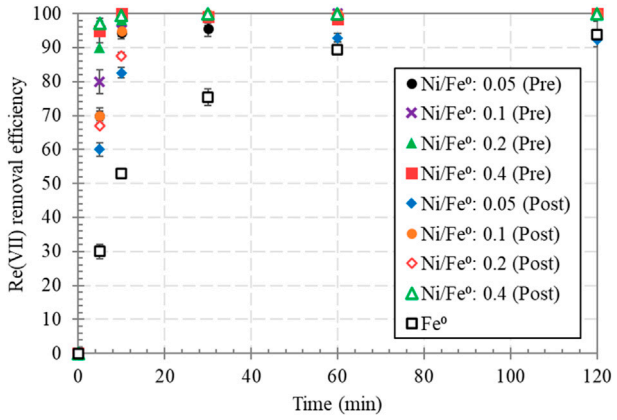

FIGURE 4
Re(VII) removal by pre- and post-nucleation synthesized Ni/Fe^0 considering different Ni/Fe^0 (wt/wt) ratios (reaction conditions: 120 min contact time, 5.0 ± 0.2 initial pH, 25 ± 1.0°C temperature, 15.0 ± 0.62 μM initial Re(VII) concentration, and 1.0 g/L dosage).

$$\text{Removal efficiency (R\%)} = \frac{C_0 - C_t}{C_0} \times 100 \quad (3)$$

$$\text{Uptake equilibrium capacity } (q_e) = \frac{(C_0 - C_e)V}{m} \quad (4)$$

where R (%) is removal efficiency, q_e (mg/g) is uptake equilibrium capacity, C_0 (mg/L), C_t (mg/L), and C_e (mg/L) denote the initial, time (t)-corresponding, and equilibrium Re(VII) concentrations, respectively, V is the solution volume (L), and m stands for the mass of Fe^0 or Ni/Fe^0 (g).

2.6 Experimental data modeling

To evaluate the kinetic behavior of Re(VII) removal by Fe^0 and Ni/Fe^0, experimental data were fitted using pseudo-first-order, pseudo-second-order, intra-particle diffusion, and Elovich kinetic models (Aharoni and Sparks, 1991; Wu et al., 2009; Maamoun et al., 2021; Falyouna et al., 2022).

Pseudo-first-order model:

$$q_t = q_e\left(1 - e^{-k_1 t}\right) \quad (5)$$

Pseudo-second-order model:

$$q_t = \frac{q_e^2 k_2 t}{1 + q_e k_2 t} \quad (6)$$

Intra-particle diffusion model:

$$q_t = k_{int} t^{0.5} + C_{int} \quad (7)$$

Elovich model:

$$q_t = \frac{1}{\beta}\ln(\alpha\beta t + 1) \quad (8)$$

where q_t (mg/g) represents Re(VII) uptake by a mass unit of either Fe^0 or Ni/Fe^0 at a predetermined time t (min); k_1 (1/min) is the pseudo-first-order kinetic rate constant; k_2 (g/mg min) is the pseudo-second-order kinetic rate constant; k_{int} (mg/g min$^{0.5}$) is the intra-particle diffusion rate constant; C_{int} (mg/g) is a constant that represents the boundary layer thickness, β (mg/g min) is Elovich initial kinetic rate constant, and α (g/mg) is Elovich kinetic rate constant.

For further interpretation of the reaction temperature effect on Re(VII) removal, investigation on uptake thermodynamics is crucial. The thermodynamic parameters were determined *via* the following equations (Kumar et al., 2011; Ghosal and Gupta, 2015; Ahmad et al., 2016).

$$\Delta G = -RT\ln K_e \quad (9)$$

$$\Delta G = \Delta H - T\Delta S \quad (10)$$

$$\ln K_e = \Delta S/R - \Delta H/RT \quad (11)$$

Where ΔG is Gibbs free energy change (kJ/mol), ΔH is enthalpy change (kJ/mol), ΔS is entropy change (J/mol K), T is the temperature in K, and R is the universal gas constant (8.314 J/mol K), and K_e represents equilibrium constant (approximately estimated from products/reactants concentrations ratio in equilibrium reactions at different temperatures).

Adsorption isotherm curves are useful for analyzing the interaction between adsorbent and adsorbate as well as the properties of the adsorption layer. Langmuir, Freundlich, and Sips (modified Langmuir/Freundlich) adsorption isotherm models were used and described in the following equations (Ayawei et al., 2017; Maamoun et al., 2021; Eljamal et al., 2022b).

Langmuir isotherm model:

$$q_e = \frac{q_{\max\,(L)} K_L C_e}{1 + K_L C_e} \quad (12)$$

Separation factor:

$$R_L = \frac{1}{1 + K_L C_0} \quad (13)$$

Freundlich isotherm model:

$$q_e = K_F C_e^{1/n} \quad (14)$$

Sips isotherm model:

$$q_e = \frac{q_{\max\,(s)} K_s C_e^{n_s}}{1 + K_s C_e^{n_s}} \quad (15)$$

Where $q_{max(L)}$ (mg/g) stands for Langmuir maximum adsorption capacity; The Langmuir constant associated with adsorption energy is K_L (L/mg); The separating factor is R_L: R_L = 1, linear; R_L = 0, irreversible; R_L > 1, unfavorable; 0 < R_L < 1, favorable. K_F is the Freundlich constant [(mg/g) (L/mg)$^{1/n}$], while 1/n is the adsorption affinity constant.

The coefficient of determination (R^2) was used to determine the best-fitting models. Moreover, the well-known Akaike Information Criterion (AIC) model was considered for investigating the goodness of fit for all the applied models (Kumar et al., 2011; Eljamal et al., 2022a; Maamoun et al., 2022a):

$$\text{AIC} = 2K + N\ln\left[\frac{SSE}{N}\right] + \frac{2K(K+1)}{N - K - 1} \quad (16)$$

Where K is the number of the independently adjusted parameters in the applied model, N is the number of

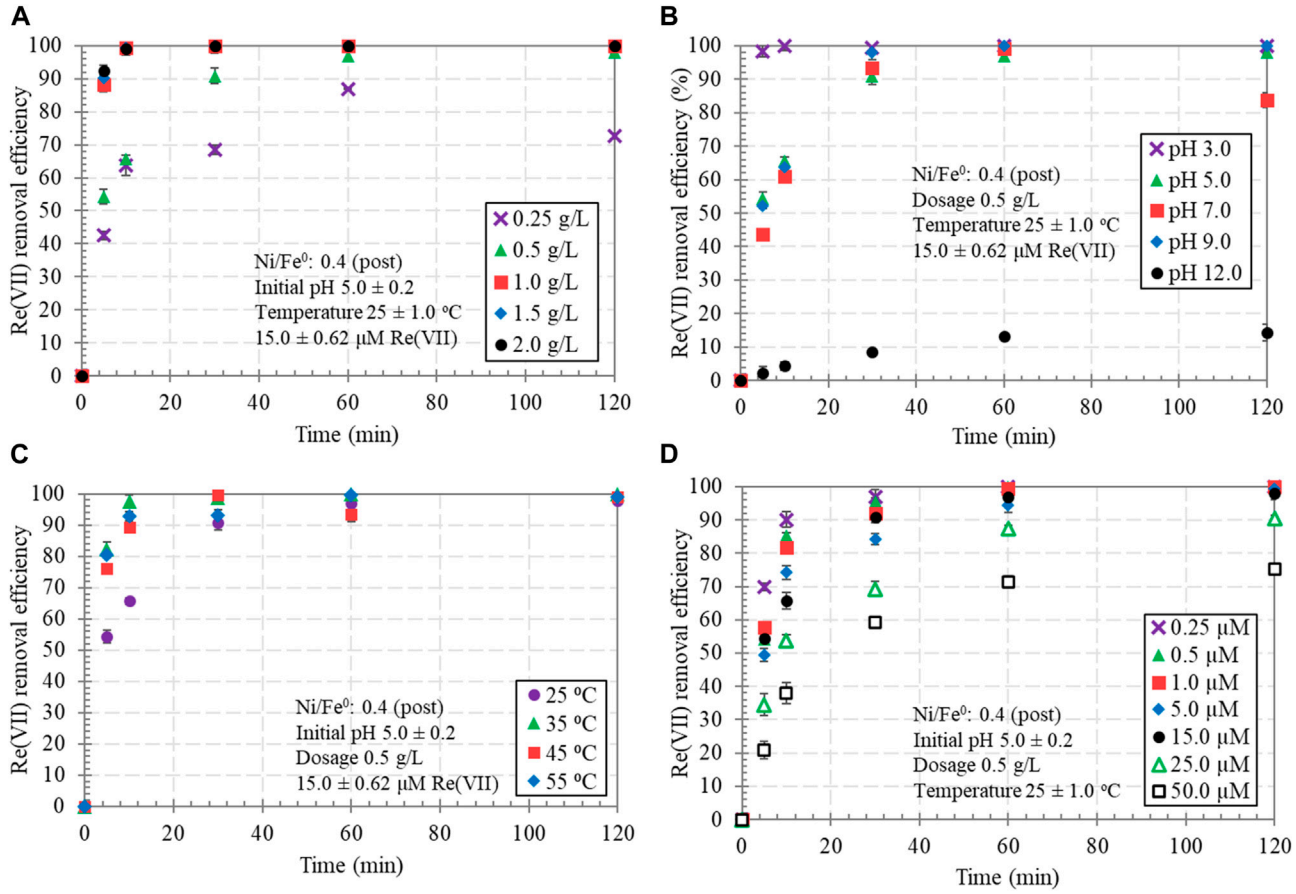

FIGURE 5
Re(VII) removal by Ni/Fe^0: 0.4 (post-nucleation), considering the effect of: dosage **(A)**, initial pH **(B)**, reaction temperature **(C)**, and initial Re(VII) concentration **(D)** (120 min contact time).

experimental measurements, and SSE is the sum of squared errors between the experimental (q_{exp}) and calculated (q_{calc}) uptake capacities, which can be estimated by the following formula.

$$SSE = \sum_i^N \left(q_{exp} - q_{calc}\right)_i^2 \quad (17)$$

The lower the AIC value, the better the fitting of the model to the experimental data. So, the model with the lowest AIC value shall be chosen to describe the data. Non-linear modeling was considered for the kinetic and isotherm modeling as it showed higher accuracy and to avoid the errors resulting from non-linear/linear transformation in terms of error structure, error variance, and normality assumptions of the standard least squares (Taguba et al., 2021; Falyouna et al., 2022).

3 Results and discussion

3.1 Characterization

XRD analysis was conducted for fresh and spent (after reaction with Re(VII)) Fe^0 and Ni/Fe^0, as shown in Figure 1. The determination of XRD peaks and structure phases in the obtained patterns were conducted based on the X-ray diffraction opensource database of American Mineralogist Crystal Structure (AMCSD), and the previously reported XRD diffraction data of International Centre for Diffraction (JCPDS). Fresh Fe^0 exhibited the typical major peaks at 2θ of 44.8° (110) and 82.4° (211), in agreement with previously reported studies (AMCSD 0000670, and JCPDS No. 006–0,696) (Wu et al., 2017; Maamoun et al., 2022b, 2023b). After the reaction with Re(VII), Fe^0 major peak was slightly shifted (2θ of around 0.26°) to yield the structure phase of Fe (111) at 2θ of 45.06° (AMCSD 0019422), similar to what was previously observed at different reaction time (Zhang and Wang, 2019). Oxidation of Fe^0 after reaction with Re(VII) was confirmed by the presence of magnetite (Fe_3O_4) peaks at 2θ of 30.6° (220), 35.8° (311), 56.9° (333), 62.6° (440), and hematite (Fe_2O_3) at 33.2° (104), 54.1° (116), following JCPDS No. 01–088–0,315 and AMCSD 0002400 (magnetite) and JCPDS No. 01–073–2,234 and AMCSD 0000143 (hematite) (Shagholani et al., 2015; Yan et al., 2019). It is worth mentioning that some iron oxides peaks in the spent Fe^0 implied the presence of ReO_2 peaks. The XRD pattern of the freshly synthesized Ni/Fe^0 exhibited similar Fe^0-major peaks to the fresh Fe^0 material, in addition to the several peaks associated with NiO (220) (AMCSD 0011371), $NiFe_2O_4$ (311), (422) (511) (AMCSD 0015511), and Fe-Ni (112) (AMCSD 0000787) (Jing et al.,

TABLE 1 Thermodynamic parameters of Re(VII) removal by Ni/Fe^0.

Temperature (K)	△G (kJ/mol)	△H (kJ/mol)	△S (J/mol K)	E_a* (kJ/mol)
298.15 (25°C)	−37.12	25.72	124.57	33.92
308.15 (35°C)	−38.36			
318.15 (45°C)	−39.61			
328.15 (55°C)	−40.85			

*Activation energy.

2016; Kerli and Soğuksu, 2019). The expected reduction of Ni^{2+} to Ni^0 was confirmed by the presence one peak associated with Ni (111), indicating the possibility of the partial reduction of Ni^{2+} to Ni^0 by Fe^0, which can be attributed to the post-nucleation method (agitating time could not be enough to transform all Ni^{2+} species to the zero-valent form). While in the case of the spent Ni/Fe^0, almost the same pattern was observed, except for the presence of some new iron oxides peaks (Fe_3O_4(511) (440)) (Jing et al., 2016; Kerli and Soğuksu, 2019). The presence of ReO_2 peaks in Ni/Fe^0 spent pattern (110) (111) (AMCDS 0011771), and Fe-O-Re complexes (110) (201), (403) (AMCDS 0016387), confirmed the successful reduction of Re(VII) to Re(IV) and the possible formation of Fe-Re co-precipitates (Li et al., 2016; Fu et al., 2020; Tang et al., 2020). Nevertheless, there was no clear attribution for the change of Re(IV) peaks position within the two spent materials.

Unlike the post-nucleation synthesis approach, pre-nucleation synthesis of Ni/Fe^0 nanoparticles resulted in an almost full reduction of Ni^{2+} to Ni^0, represented by Ni peaks (111, and 220) and Fe-Ni (bcc) (002) (300), and (112), in addition to the typical Fe^0 peaks (Sahoo et al., 2005; Chandra et al., 2014; Yung et al., 2014; Jing et al., 2016) (Supplementary Figure S1). Such observations depicted the difference between the pre- and post-nucleation synthesis approaches, in terms of the Ni state within the Ni/Fe^0 material.

STEM imaging was conducted for Fe^0 and Ni/Fe^0: 0.4 (post), as displayed in Figure 2. Both Fe^0 and Ni/Fe^0 had the typical chain-like aggregated form, with particle size ranges of 8—156 and 12—124 nm, respectively (obtained by image analysis using ImageJ software). A well-defined spherical shape was observed in the case of fresh Fe^0, while Ni/Fe^0 showed a less uniform shape, confirmed by STEM images of the low magnifying scale (Supplementary Figure S2A). Such observations could be related to the post-synthesis Ni-doping on the surface of Fe^0, which may have caused some changes to the spherical shape of the particles. The black iron core was observed in most of Fe^0 and Ni/Fe^0 particles with no sign of the bright passivation oxide clouds. EDS elemental mapping confirmed that Ni was well-distributed within Ni/Fe^0 particles, represented by Ni peaks in the EDS spectrum. Non-related peaks of EDS (e.g., carbon (C), and copper (Cu)), were attributed to TEM Cu-grid material and the supporting film included. After normalizing the EDS elemental content, Fe content was ~89.96%, and ~90.01% in Fe^0 and Ni/Fe^0, respectively. Spent Ni/Fe^0 showed a deformed-spherical shape with thin clouds around the black iron core, attributed to the passivation layer involved in Re(VII) removal (Supplementary Figure S2B). Nevertheless, Re was not detected in the EDS analysis of the spent Ni/Fe^0 (Supplementary Figure S2), which could be related to the relatively low initial concentration (15.0 ± 0.62 μM), unlike the higher concentration in the case of XRD. Hence, the absence of detected Re in EDS analysis does not necessarily reflect the efficiency of Re(VII) removal, which was confirmed by other characterization techniques, as will be discussed.

Fe K-edge XANES spectra of Fe reference materials (i.e., Fe foil, Fe(II) [FeO], and Fe(III) [Fe_2O_3]), fresh and spent Fe^0 and Ni/Fe^0 are displayed in Figure 3A. No clear difference was observed in XANES spectra between the fresh and spent status of both Fe^0 and Ni/Fe^0, indicating that Fe oxidation state was not greatly changed. Although the preparation process of the solid samples was prepared inside a glove box, the possibility of air oxidation cannot be totally eliminated, knowing that the process involved several steps, including vacuum filtration, solid-phase dilution (involving mixing), and packing. Intensity differences were observed between Fe^0 and Ni/Fe^0 materials at some energy regions (e.g., 7,107—7,130 eV, and 7,090—7,106 eV). The change in the peak intensity and position can be caused by two main reasons; firstly, the direct linking between the number of atoms and the respective oxidation state, as it is proportional to atoms on the respective chemical state. Secondly, the change in the intensity depends on the depth distribution of the atoms, where increased intensity reflects atomic diffusion towards the surface, and decreased intensity when atoms diffuse towards the bulk (Powell et al., 2001). The fitting analysis of the obtained spectra indicated that Fe^0 and Ni/Fe^0 materials yielded peaks patterns close to that of Fe foil reference, at 7,092—7,095 eV, and about 7,111.78 eV. Fe(II) broad peak was observed in Fe^0 and Ni/Fe^0 materials at about 7,110.79 eV, while Fe(III) peaks at about 7,113.66 and 7,127.25 eV were totally suppressed (Mardare et al., 2012; Grillet et al., 2014; Liu et al., 2019, 2021). Such results indicated that Fe oxidation state in both Fe^0 and Ni/Fe^0 materials involved both Fe^0 and Fe(II) states, reflecting the partial oxidation of Fe^0-core and the involvement of Fe^0, as an electron donor, in the reductive immobilization of Re(VII). These observations were in agreement with the findings from XRD patterns implying that the majority of the magnetite peaks are related to Fe(II).

Ni K-edge XANES analysis was conducted using Ni reference materials (i.e., Ni metallic foil, Ni metallic powder, Ni(II) [NiO], and Ni(II) [$Ni(OH)_2$]), fresh and spent Ni/Fe^0. As shown in Figure 3B, fresh and spent Ni/Fe^0 showed almost identical spectra with a mixed oxidation state of Ni^0 and Ni(II). Ni/Fe^0 materials showed peaks close to that of Ni foil and metallic Ni at 8,312—8,324 eV and 8,327—8,332 eV, in addition to peaks close to that of NiO and $Ni(OH)_2$ at 8,325—8,340 eV (Beale et al., 2009; Tirez et al., 2011). While the peaks associated with NiO at about 8,348.25 and

8,381.92 eV, and $Ni(OH)_2$ at about 8,377.94 eV were quenched in the case of Ni/Fe^0 materials (Beale et al., 2009; Tirez et al., 2011). Linear combination fitting was used as fitting analysis and ratio quantification tool of XANES spectra (REX2000 software ver. 2.5.9, Co. Ltd., Japan). The results of the fitting analysis of the formerly discussed spectra depicted that the highest fitting spectra corresponding to Ni/Fe^0 materials were Ni foil and NiO, with Ni to NiO ratio of Ni (60%) + NiO (40%) and Ni (66%) + NiO (34%) for fresh and spent Ni/Fe^0, respectively (Supplementary Table S1). These findings indicated that the majority of Ni was presented in the fresh Ni/Fe^0 as a metallic form. After the reaction with Re(VII), no significant difference was observed in the oxidation state of Ni, indicating that low possibility of Ni^0 contribution in Re(VII) reduction.

Re L_{III}-edge XANES analysis has been conducted using Re reference materials (i.e., Re(VII) [NH_4ReO_4], Re(IV) [ReO_2], and Re(III) [$K_3(ReCl_6)$]), spent Fe^0 and Ni/Fe^0 to determine Re oxidation state in the reacted solid materials after the reaction. As shown in Figure 3C, XANES spectra of spent Fe^0 and Ni/Fe^0 exhibited peaks shifted from that of Re(VII) reference, and close to that of Re(IV) and Re(III) references at a photon energy of about 10,528.67 eV (Takahashi et al., 2007; Tougerti et al., 2012; Karanjkar et al., 2016). Furthermore, the shoulder of Re(VII) at about 10,542.02 eV was quenched in spent Fe^0 and Ni/Fe^0, similar to the Re(IV) and Re(III) references. These results suggested that Re oxidation state was totally dissimilar to Re(VII), indicating the successful reductive immobilization of Re(VII) to lower oxidation states by both Fe^0 and Ni/Fe^0. It is worth mentioning that in the case of using Ni/Fe^0 with lower Re concentration, the obtained XANES spectrum was almost identical to the Re(III) standard, indicating the full reduction of Re(VII) to Re(III), which indicates the possible Re co-precipitation on the surface of the spent sample as Re(III) (Supplementary Figure S3). Such observations were supported with the results of linear combination fitting, exhibiting Re(III) (82%) + Re(IV) (18%) and Re(III) (100%) + Re(IV) (0%) for spent Fe^0 and Ni/Fe^0, respectively (Supplementary Table S2, Supplementary Table S3).

3.2 Re(VII) immobilization

3.2.1 Ni/Fe^0 optimization

Batch experiments were conducted to evaluate the efficiency of Fe^0 and Ni/Fe^0 in Re(VII) removal from aqueous solutions. The first stage in this work was optimizing the Ni/Fe^0 (wt/wt) ratio (0.05, 0.1, 0.2, and 0.4), in correspondence with pre- and post-nucleation synthesis approaches. As shown in Figure 4, 1.0 g/L of Fe^0 could remove ~30% of initial 15 μM Re(VII) concentration within the first 5 min of the reaction, and ~94% final removal efficiency. Meanwhile, all Ni/Fe^0 materials, regardless the Ni/Fe^0 ratio and the synthesis approach, showed higher removal performance than Fe^0, especially in the early stage of the reaction (5—30 min).

It was clear that the higher the Ni content in Ni/Fe^0, the faster the kinetic rate of Re(VII) removal, where pre- and post-nucleation synthesized Ni/Fe^0: 0.4 exhibited the best removal performance with more than 97% within just 5 min of the reaction time. Such an improved kinetic rate can be attributed to: (1) the catalytic added-value of Ni, which yielded Ni/Fe^0 with a highly reactive surface, (2) the possible involvement of Ni^0 (reduced by Fe^0, Equation 18 (Zhang et al., 2012)) in Re(VII) reduction to lower oxidation states, and (3) the contribution of the doped-Ni in providing an efficient medium for better electron transfer from Fe^0-core to Re(VII) aqueous species. Nevertheless, the involvement of Ni^0 in Re(VII) reduction was not clearly confirmed, owing to the aforementioned XANES results, as well as the fact that Fe^0 is a stronger reducing agent than Ni^0 (Equations 19 and 20) (Alia et al., 2012; Rosser et al., 2016; Penke et al., 2019). Hence, Fe^0 could have been dominant in reducing Re(VII) to Re(IV)/Re(III). Slight superiority was observed for post-nucleation to the pre-nucleation, associated with the mixed surface of Ni^0/NiO in the case of the post-nucleation approach, which could have enhanced the electron transfer; as metal oxides are well-known promising mediums for electron transfer (Azcarate et al., 2018; Möllmann et al., 2020). While in the case of pre-nucleation approach, Ni^0 was the major component of on Fe^0-surface as suggested by XRD results. Hence, Ni/Fe^0: 0.4 (post) was considered for further Re(VII) removal experiments.

$$Fe^0 + Ni^{2+} \rightarrow Fe^{2+} + Ni^0 \quad (18)$$

$$Fe^{2+} + 2e^- \rightarrow Fe^0 \quad (E^0 = -0.44\,V) \quad (19)$$

$$Ni^{2+} + 2e^- \rightarrow Ni^0 \quad (E^0 = -0.25\,V) \quad (20)$$

3.2.2 Dosage effect

Several Ni/Fe^0 dosages (0.25, 0.5, 1.0, 1.5, and 2.0 g/L) were investigated for Re(VII) removal from water, as shown in Figure 5A. Results indicated that even at the lowest dosage (0.25 g/L), ~87% Re(VII) removal efficiency was achieved after 1 h reaction time. The slight decline in removal efficiency after 2 h (~73%) could be related to the possible occurrence of desorption at the late stage of the reaction (detachment of physically adsorbed Re(VII) species). As expected, Re(VII) removal efficiency increased with increasing Ni/Fe^0 dosage, to reach almost full removal efficiency at the end of the reaction (after 2 h) for a wide range of dosage (0.5—2.0 g/L).

The results of kinetic analysis for Re(VII) removal showed that the reaction was well-described by both pseudo-first- and second-order models, with a clear superiority to the former in the case of dosage investigation. These findings implied that Re(VII) removal process by Ni/Fe^0 involved both physical and chemical mechanisms. The best-fitting model was decided based on the highest coefficient of determination (R^2) and the lowest AIC values (Supplementary Table S4). Comparing the same dosage of 1.0 g/L introduced to the Re(VII)-saturated solution, Ni/Fe^0 yielded a much higher kinetic rate constant than Fe^0 with ~82% and ~94% increase in pseudo-first- and second-order kinetic rate constants, respectively. Ni/Fe^0 dosages ≥1.0 g/L had the highest kinetic rates constants, indicating that 1.0 g/L Ni/Fe^0 could be more than efficient in achieving rapid and full Re(VII) removal. Nevertheless, it was necessary to consider a lower dosage (0.5 g/L) in the rest of the experiments to elucidate the actual effect of other reaction parameters.

3.2.3 Initial pH effect

The effect of initial pH on Re(VII) removal by Ni/Fe^0 was studied, considering a pH range from 3.0 to 12.0. As shown in Figure 5B, Re(VII) removal was significantly induced at acidic conditions, unlike the alkaline. Such observations can be

TABLE 2 Adsorption isotherm parameters of Re(VII) removal by Ni/Fe^0.

Isotherm model	Parameter (unit)	Value
Langmuir	K_L (L/mg)	8.790
	$q_{max(L)}$ (mg/g)	13.24
	R^2	0.975
	AIC[a]	9.414
Freundlich	K_F [(mg/g) (L/mg)$^{1/n}$]	10.98
	n	3.5
	R^2	0.997
	AIC	−7.225
Sips	K_s (L/g)	0.102
	n_s	0.307
	$q_{max(s)}$ (mg/g)	118.6
	R^2	0.997
	AIC	−0.180

[a]Akaike Information Criterion.

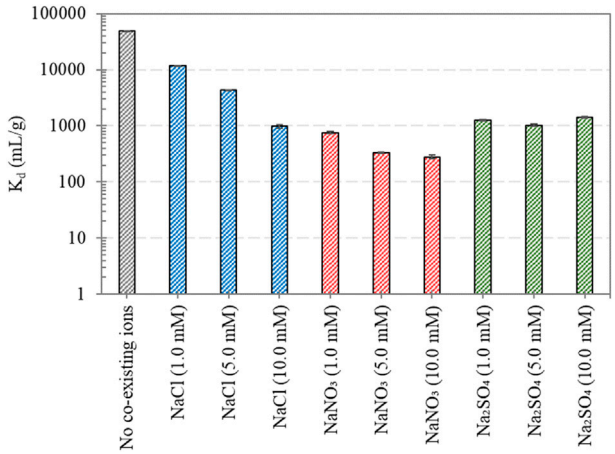

FIGURE 6
Re(VII) removal by Ni/Fe^0: 0.4 (post-nucleation) at different concentrations of co-existing ions (reaction conditions: 120 min contact time, 5.0 ± 0.2 initial pH, 25 ± 1.0°C temperature, 15.0 ± 0.62 μM initial Re(VII) concentration, and 0.5 g/L dosage).

attributed to the following reasons: (1) the acidic pH conditions induced the rapid oxidation of Fe^0-core, resulting in faster release of electrons required for Re(VII) reduction, (2) the acidic conditions decrease the insoluble reaction products on Ni/Fe^0 surface, and (3) the role of electrostatic attraction of negatively charged Re(VII) species to the positively charged surface of Ni/Fe^0 would fade approaching towards the alkaline conditions (pH 12.0). Zeta potential measurements (Zeta sizer NanoSeries, Malvern Panalytical Ltd, UK) were conducted to check the possible involvement of electrostatic sorption in Re(VII) removal process. Results depicted that the point of zero charge of Fe^0 and Ni/Fe^0 was determined at pH_{PZC} of 8.24 and 7.63, respectively (Supplementary Figure S4). Such results suggested the aforementioned attributions and the involvement of electrostatic sorption of ReO_4^- (the dominant Re(VII) species) on the positively charged surface of Ni/Fe^0 at acidic and neutral conditions (Nikolaychuk, 2022). Contrarily, alkaline conditions were not favorable for Re(VII) removal due to the electrostatic repulsion as well as the low-tendency of Re(VII) reduction caused by the delayed Fe^0-core oxidation. Such Re(VII) reduction inhibition effect at alkaline conditions was previously reported, owing to the same attributions in the present work (Lenell and Arai, 2017). Meanwhile, Ni/Fe^0 could efficiently remove Re(VII) within a wide pH range (3.0—9.0), indicating the high applicability of the material in different environmental conditions. The observations of kinetic rate constant values indicated that the kinetic rate of Re(VII) removal increased with the decrease of the initial pH (Supplementary Figure S4).

$$Fe^0 + 2H_2O \rightarrow Fe^{2+} + H_2 + 2OH^- \quad (21)$$

Re(VII) solutions were purged with Ar gas before starting the experiments, to ensure a very low level of dissolved oxygen (<1.0 mg/L). Hence, upon introducing Ni/Fe^0 material to the reaction, water was the predominant electron receptor, causing iron oxidation reaction (Eq. (21)) (Wei et al., 2010; Shi et al., 2011). Such a reaction resulted in a typical increase in solution pH and a significant decline in redox potential (Supplementary Figure S5). ORP values significantly decreased within Ni/Fe^0 reaction with Re(VII), reflecting the strong reducing environment provided for Re(VII) reduction. Correspondingly, the progressive decline of ORP values was consistent with the associated progression of the reduction process, which required time and high activation energy as a chemical process.

3.2.4 Temperature effect

The effect of reaction temperature on Re(VII) removal by Ni/Fe^0 was investigated considering a range from 25 to 55°C. As displayed in Figure 5C, it was clear that 0.5 g/L Ni/Fe^0 could efficiently remove Re(VII), achieving almost 100% final removal efficiencies at all investigated temperatures. Such results provided further proof of the high applicability of the proposed material to be used under different environmental conditions. The kinetic removal rate was enhanced by increasing reaction temperature, which was clearly observed at values >25°C, and confirmed by the obtained values of kinetic rate constants (Supplementary Table S4). The thermodynamic analysis represents the cornerstone for understanding the effect of reaction temperature on the removal processes of contaminants. Hence, thermodynamic parameters of Re(VII) removal by Ni/Fe^0 were estimated, as displayed in Table 1; Supplementary Figure S6. The positive sign of enthalpy change ($\Delta H > 0$) demonstrated that Re(VII) reaction with Ni/Fe^0 had an endothermic nature and that the removal process was favored at higher temperatures. Furthermore, the positive sign of entropy change ($\Delta S > 0$), indicated the irreversibility of the removal process. Additionally, the negative sign of the change in Gibbs free energy ($\Delta G < 0$) indicated that the reaction proceeded spontaneously in the forward direction to form more products (favorable reaction). It has been previously reported that ΔG value may demonstrate the type of sorption process; whether

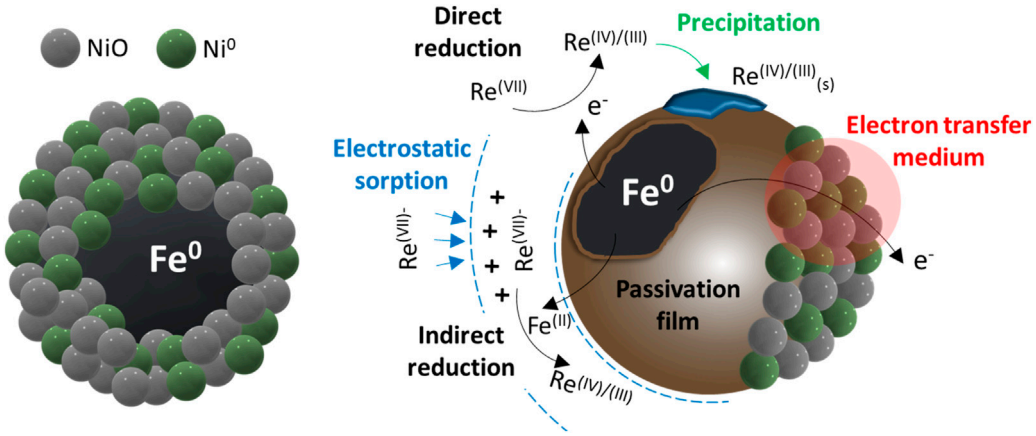

FIGURE 7
Removal pathways of Re(VII) removal by Ni/Fe^0.

physisorption (2.0 kJ/mol < ΔG < 20 kJ/mol), physisorption/chemisorption (20 kJ/mol < ΔG < 80 kJ/mol), or chemisorption (80 kJ/mol < ΔG < 400 kJ/mol) (Saha and Chowdhury, 2011; Tran et al., 2016). Hence, the temperature-correspondent values of ΔG implied the two physisorption and chemisorption pathways in Re(VII) removal by Ni/Fe^0, indicating the possible involvement of electrostatic sorption with reduction in the removal process. Moreover, the magnitude of ΔH may give another indication to the type of sorption; where physisorption (ΔH < 20 kJ/mol), or chemisorption (80 kJ/mol < ΔH < 200 kJ/mol) (Saha and Chowdhury, 2011). Therefore, the magnitude of ΔH (25.72 kJ/mol) supported the involvement of physisorption. Detailed information on thermodynamic calculations is provided in Supplementary Figure S5. Activation energy of Re(VII) removal process by Ni/Fe^0 was calculated *via* Arrhenius formula (Ahmad et al., 2014).

$$\ln k_2 = \ln k_0 - \frac{E_a}{RT} \tag{22}$$

where k_2 represents the pseudo-second-order kinetic rate constant (g/mol min), k_0 is Arrhenius factor which represents the sorption rate constant (g/mol min), and E_a is the sorption activation energy (J/mol). Plotting ln k_2 against 1/T yielded a straight line with a slope of–E_a/R (Supplementary Figure S7). The calculated Ea for Re(VII) removal by Ni/Fe^0 was 33.92 kJ/mol (<40 kJ/mol), indicating that the removal process involves a physisorption mechanism (Baek et al., 2010). Detailed information on activation energy calculations is provided in Supplementary Figure S6.

3.2.5 Initial Re(VII) concentration effect

The initial concentration effect on Re(VII) removal by Ni/Fe^0 was studied considering different values (0.25, 0.5, 1.0, 5.0, 15.0, 25.0, and 50.0 μM). The results clearly indicated the potential of Ni/Fe^0 to satisfactorily remove Re(VII), even at very high initial concentrations, where it exhibited final removal efficiency of ~75% and ~90% of 50.0 and 25.0 μM initial Re(VII) concentrations, respectively (Figure 5D). While at lower initial concentrations, much better removal performance was observed with a nearly full removal efficiency for 0.25, 0.5, 1.0, 5.0, and 15.0 μM. The decrease in reaction rate constant with increasing Re(VII) initial concentration were expected (Table 1, Supplementary Material), due to the possible accumulation of Re(IV)-precipitates on Fe^0 surface resulting in a surface blocking effect, which was in agreement with previously reported work (Ding et al., 2013). Adsorption isotherm models were used to further investigate the type of sorption processes involved in Re(VII) removal by Ni/Fe^0. As exhibited in Table 2; Supplementary Figure S8, both Freundlich and Sips isotherm models had similar R^2 value of 0.997, higher than that of the Langmuir model (0.975). However, slight superiority was observed for the Freundlich model, exhibiting the lowest AIC value (−7.225). Such findings indicated that the removal process involved a physicochemical mechanism (multi- or mono-layer sorption) with a significant contribution of electrostatic sorption. Such results agreed with the aforementioned interpretations of kinetics and thermodynamic analyses. Additionally, the parameter (n) of the Freundlich model was higher than 1, indicating the strong affinity between Re(VII) species and the heterogeneous binding sites on Ni/Fe^0 surface. Meanwhile, the calculated separation factor R_L values from the Langmuir model at different temperatures and initial concentrations were in the range from 0 to 1, verifying that removal process involved outer sphere adsorption, attributed to the physical attraction with relatively weak Van der Waal's forces resulting in weakly bound complexes (Supplementary Table S7). The involvement of physical adsorption through outer-sphere surface complexes was supported with the SEM-EDS elemental mapping of Fe^0 and Ni/Fe^0 spent samples, which exhibited the distribution of the adsorbed Re on the surface of the samples (Supplementary Figure S9). R_L values increased (approaching to 1) at higher temperatures, except for a drop at 45°C related to the slight decline in Re(VII) removal in the experimental data. Nevertheless, it would not affect the endothermic nature of the removal process. Furthermore, Ni/Fe^0 exhibited a maximum uptake capacity ($q_{max(sips)}$) to Re(VII) of 118.6 mg/g, which was higher than most of the previously reported iron-based sorbents (Li et al., 2016, 2019; Fu et al., 2020).

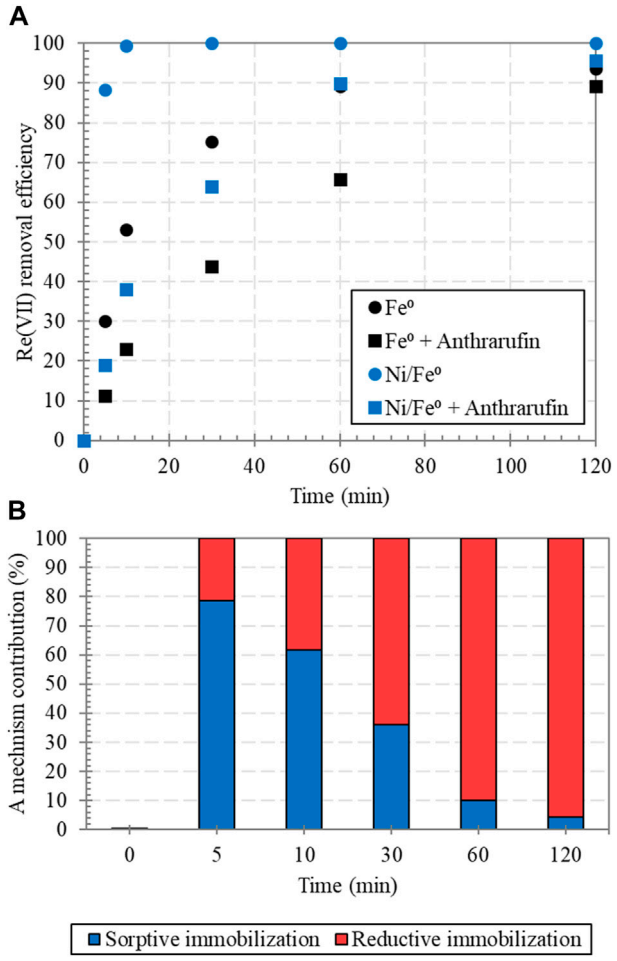

FIGURE 8
Effect of Fe(II)-chelating agent (Anthrarufin or 1,5-dihydroxyanthraquinone: 2.0 mM) on Re(VII) removal by Fe^0 and Ni/Fe^0: 0.4 (post-nucleation) **(A)**, and mechanisms contribution in Re(VII) removal by Ni/Fe^0 **(B)** (reaction conditions: 120 min contact time, 5.0 ± 0.2 initial pH, 25 ± 1.0°C temperature, 15.0 ± 0.62 μM initial Re(VII) concentration, and 1.0 g/L dosage).

3.2.6 Co-existing ions effect

The effect of competing anions on Re(VII) removal by Ni/Fe^0 was investigated, considering different concentrations (1.0, 5.0, and 10.0 mM) of NaCl, $NaNO_3$, and Na_2SO_4. Distribution coefficient ($K_d = q_e/C_e$) of Re(VII) removal by Ni/Fe^0 was estimated at different conditions of anionic medium. As shown in Figure 6, the K_d value for Re(VII) removal by Ni/Fe^0 in ultrapure water with 15.0 ± 0.62 μM initial Re(VII) concentration and at 5.0 ± 0.2 initial pH was ~48,469 mL/g. It is worth mentioning that such a high K_d value of Ni/Fe^0 was one order of magnitude higher than other reported adsorbents, such as magnesium aluminum layered double hydroxide (Mg-Al LDH), and nickel-zinc layered hydroxide salt (Ni-Zn LHS), which needed longer equilibrium time and yielded less K_d value of Re(VII) removal in salt free solution (Tanaka et al., 2019b, 2019a). Results indicated that K_d values decreased with the presence of competing anions (i.e., Cl^-, NO_3^- and SO_4^{2-}). Among the competing anions, Cl^- had the least influence on Re(VII) removal, yet the effect increased with increasing anionic concentration to reach ~968 mL/g at 10 mM Cl^- concentration. Meanwhile, the effect of NO_3^- and SO_4^{2-} on Re(VII) removal was higher than that of Cl^-, exhibiting K_d values of ~279 and ~1,408 mL/g at 10 mM NO_3^- and SO_4^{2-} concentrations, respectively. The initial and final pH measurements of the conducted experiments implied the increase in the final pH of the solution with the presence of co-existing ions, compared with that ay their absence (Supplementary Figure S10). Such pH observations can be interpreted by the involved mechanism of these anions in the Ni/Fe^0-Re reaction system. For instance, the reduction reaction of NO_3^- by Fe^0 to form NH_4^+ increases the OH^- in the system, causing the rise in the solution pH (Lenell and Arai, 2017). Hence, the observed increase in the final pH supported the NO_3^- reduction hypotheses, which influenced the overall Re(VII) reduction performance by the competition over Fe^0-electrons. The final nitrate concentration in the solution was measured, and showed great depletion at the three different initial nitrate concentrations (1.0 mM → 0.27 mM, 5.0 mM → 0.57 mM, and 10.0 mM → 0.61 mM); supporting the increase in final pH due to nitrate reduction. There is a gap in the literature on the reported studies investigating the effect of competing ions on Re(VII) or Tc(VII) removal by Fe^0-based materials. Nevertheless, several reports suggested the high sensitivity of Re(VII) removal by other materials to NO_3^- and SO_4^{2-} competing anions, including Mg-Al LDH, and Ni-Zn LHS, where adsorption was the main governing mechanism (Komarneni et al., 1996; Tanaka et al., 2019a, 2019b). Also, Sheng et al. reported the high influence of SO_4^{2-} on Re(VII) immobilization by Fe^0 and Fe^0-LDH; however, the exact concentration of the competing anions was a bit ambiguous (Sheng et al., 2016). Such results suggested the dependency of Re(VII) removal by Ni/Fe^0 on the concentration and type of the competing anions, and can be attributed to the reciprocal relation between the concentration of competing anions and the reactivity of Ni/Fe^0. At high concentrations of competing anions, there was a high possibility of blocking the active sites on Ni/Fe^0 surface by the complexes formed from co-precipitation of iron oxides with the anionic species (Sheng et al., 2016). While at low concentrations, the iron oxyhydroxide passivation shell can be easily dissolved without opposing precipitates (Kim et al., 2014; Sheng et al., 2016).

3.3 Re(VII) removal pathways

Based on the aforementioned discussion on the characterization of Re-loaded spent materials and the modeling of experimental data, the following pathways can be suggested for Re(VII) removal by Ni/Fe^0 (summarized in Figure 7).

(1) Electrostatic attraction of negatively charged ReO_4^- on the positively charged surface of Ni/Fe^0 (rapidly occurring interaction, no activation energy required) (Türk, 2014). Such a physisorption process was mostly guaranteed in most of the conducted experiments owing to the dominance of ReO_4^- in a broad pH range, and the suitable pH_{PZC} of Ni/Fe^0 (7.63) that provided the positively charged surface.
(2) Reduction of Re(VII) to Re(IV)/Re(III) by the released electrons from Fe^0-core (direct reduction), and by Fe(II) (indirect reduction). Such a chemical process progressively occurred owing to the high activation energy required. The reductive immobilization was confirmed by the absence of Re(VII) species in the spent Ni/Fe^0 XANES spectrum and XRD pattern.

Nevertheless, the absence of Re(VII) species did not necessarily depict the non-involvement of electrostatic sorption, as it could have rapidly occurred, followed by full Re(VII) reduction, causing the disappearance of Re(VII) in the spent materials.

$$3Fe^0 + 2ReO_4^- + 8H^+ \rightarrow 3Fe^{2+} + 2ReO_2 + 4H_2O \quad (23)$$

$$3Fe^{2+} + ReO_4^- + 4H^+ \rightarrow 3Fe^{3+} + ReO_2 + 2H_2O \quad (24)$$

(3) The accumulation of Re(IV)/Re(III) precipitates on the surface of the spent Ni/Fe^0, suggested by the ReO_2 peaks in XRD patterns and the full reduction of Re(VII) to Re(III) from XANES fitting results of the Ni/Fe^0 samples (low Re concentration).

(4) The role of Ni in Ni/Fe^0 could be mainly concluded in acting as a promising medium for electron transfer which facilitated the electron transfer from Fe^0-core to the aqueous Re(VII) species. Hence, it can be confirmed that the high kinetic rate of Re(VII) removal by Ni/Fe^0 in the early stage of the reaction involved both physisorption and reduction (with superiority to the fast physisorption), followed by a dominant reduction process during the rest of the reaction.

In order to confirm the contribution of sorption process in Re(VII) removal by Ni/Fe^0, an additional experiment was conducted with the presence of Fe(II)-chelating agent (Anthrarufin or 1,5-dihydroxyanthraquinone), such organic compounds have been previously reported as an effective corrosion inhibitor for metallic materials (Saqalli et al., 2018; Yang et al., 2018). As displayed in Figure 8A, Re(VII) removal by either Fe^0 or Ni/Fe^0 was significantly decreased in the presence of 1,5-dihydroxyanthraquinone. The main inhibition role of Fe(II)-chelating agent was the tight binding to Fe(II) and preventing it from acting as a catalyst for redox reactions, which caused such a depletion in Re(VII) removal. Hence, it can be depicted that the inhibition effect of Fe(II)-chelating agent was mainly oriented towards Re(VII) reductive immobilization by preventing or slowing reaction in the aforementioned Equation 24. Nevertheless, the contribution of sorptive immobilization was not prevented, that was suggested by the efficient Re(VII) removal finally achieved. Such findings provided clear evidences of: (1) reductive immobilization by electron transferred from Fe^0-core was greatly involved in Re(VII) removal by Fe^0 and Ni/Fe^0; (2) the role of Fe(II) as a catalyst in Re(VII) reduction was confirmed; (3) the contribution of reductive immobilization in Ni/Fe^0 was slightly higher than that of Fe^0, confirming the efficacy of Ni^0/NiO as a facilitating medium for electron transfer. Hence, based on these results, the time-corresponding contribution of immobilization mechanisms to Re(VII) removal by Ni/Fe^0 was empirically estimated (Figure 8B), *via* normalizing Re(VII) removal efficiency (with and without the presence of Fe(II)-chelating agent) to a percentage with respect to the ideal status (no anthrarufin), using the following empirical formulas.

$$Reductive\ immobilization\ (\%) = \frac{R\%\left(no\ anthraru\,fin\right) - R\%\left(with\ anthraru\,fin\right)}{R\%\left(no\ anthraru\,fin\right)} \times 100 \quad (25)$$

$$Sorptive\ immobilization\ (\%) = 100 - reductive\ immobilization \quad (26)$$

Sorptive immobilization showed a high contribution to Re(VII) removal within the early stage of the reaction, as a rapid physical mechanism that did not require high energy to occur. While the reductive immobilization progressively increased during the reaction, as a chemical process that needed high activation energy. Such results were consistent with the afore-discussed implications from experimental data modeling, and in good agreement with a previously reported work (Sheng et al., 2016). Nevertheless, detailed analysis of the Re oxidation state within the solution in the presence of Fe(II)-chelating agent would be critical for future investigations, for better understanding of the chelating/binding mechanism of anthrarufin and the evaluation of accessibility of the surface binding sites. Hence, as the ultimate target radionuclide, Tc(VII) can be expectedly removed by Ni/Fe^0 in rapidly and efficiently alike Re(VII) removal pathways due to the involvement of combined immobilization processes. However, it is critical to highlight the crucial factors which shall control Tc(VII) removal by Ni/Fe^0, in the light of the expected similarities and/or differences compared with Re(VII) removal. In this regard, Fe(II) content and phase shall determine the rate of Tc(VII) reduction. At circumneutral pH, the heterogenous reduction rate and extent of the aqueous Tc(VII) by the solid phase-Fe(II) is significantly induced (Cui and Eriksen, 1996; Qafoku et al., 2017). Meanwhile, within the same conditions, the homogenous Tc(VII) reduction by aqueous-Fe(II) is unlikely to occur (Zachara et al., 2007; Qafoku et al., 2017). Such observations may demonstrate the dissimilarities in Re(VII) and Tc(VII) reduction by Fe(II) phases. Furthermore, the rate of Tc(VII) reduction by Fe^0 and/or Fe(II) is significantly influenced by the pH conditions. It was previously reported that Tc(VII) reduction by Fe(II) was very slow within neutral to slightly alkaline pH conditions (Cui and Eriksen, 1996). Furthermore, significant effect of the ionic strength was observed on Tc(VII) reduction rate by iron oxides in the neutral to basic pH conditions (Vandergraaf et al., 1997; Byegård et al., 2001). Additionally, the type of electron transfer, involved in Tc(VII) reduction by Ni/Fe^0, may influence the expected reduction rates, in terms of the homogeneity/heterogeneity of electron transfer from the Fe^0-core through Ni^0/NiO electron transfer medium, and from Fe(II). Moreover, the interlayer/basal surface-exchangeability of aqueous Fe(II) in the electron transfer reaction for Tc(VII) reduction may play important role in demonstrating the involved pathway, whether homogenous reduction or regeneration for solid phase-Fe(II) (Lovley, 1993; Qafoku et al., 2017). Correspondingly, it is crucial to conduct a detailed investigation to determine the actual potential of Ni/Fe^0 material in Tc(VII) reduction.

4 Conclusion

In this study, bimetallic Ni/Fe^0 was used for rapid and efficient removal of Re(VII) from aqueous solutions. The post-nucleation synthesis approach resulted in a well-distribution of Ni and Fe within Ni/Fe^0 material, confirmed by STEM-EDS measurements. XRD patterns of the spent Ni/Fe^0 reflected the partial oxidation of Fe^0-core and the presence of ReO_2 peaks, indicating the successful reduction of Re(VII) to Re(IV). XANES results provided further evidence of the high potential of Ni/Fe^0 in the reductive immobilization of Re(VII). Ni/Fe^0: 0.4 (post-nucleation) was able to remove ~100% of 15.0 ± 0.62 μM initial Re(VII) concentration within wide pH and temperature ranges (3.0—9.0, and 25—55°C), at a low

dosage of 0.5 g/L. Furthermore, Ni/Fe^0 could achieve satisfactory Re(VII) removal at high initial concentrations (i.e., 50.0 μM: ~75%, 25.0 μM: ~90% final removal efficiencies). Kinetic modeling indicated that pseudo-first- and second-order models were the best kinetic models to describe the reaction rate of Re(VII) removal by Ni/Fe^0. Meanwhile, thermodynamic modeling depicted the endothermic nature of the reaction and the involvement of both physical and chemical processes in the removal process. Such implications were suggested by the adsorption isotherm modeling, which reflected the possibility of multi- and mono-layer sorption to occur within the removal process, following Freundlich and Sips isotherm models. Re(VII) removal by Ni/Fe^0 was governed by the reductive immobilization of Re(VII) to Re(IV)/Re(III) by the released electron from Fe^0-core, and the electrostatic sorption of ReO_4^- to the positively charged surface of Ni/Fe^0. Furthermore, the presence of Ni^0/NiO on the Fe^0-surface resulted in providing an efficient electron-transfer medium that facilitated the Re(VII) reduction leading to impressive kinetic rates. Generally, the obtained results confirmed the promising potential of the Ni/Fe^0 in Re(VII) removal from water and suggested further pilot-scale research towards its incorporation in the real applications of water treatment from Tc(VII), as the ultimate target radionuclide.

Data availability statement

The raw data supporting the conclusion of this article will be made available by the authors, without undue reservation.

Author contributions

IM: Conceptualization, Methodology, Investigation, Visualization, Software, Validation, Formal analysis, Data curation, Writing–original draft, Funding acquisition, Project administration. KT: Investigation, Writing–review and editing. TD: Investigation, Writing–review and editing. FK: Investigation. OF: Investigation, Formal analysis. OE: Investigation, Formal analysis. KT: Conceptualization, Methodology, Investigation, Resources, Writing–review and editing, Supervision, Funding acquisition.

Funding

This research was funded by Environmental Radioactivity Research Network Center (ERAN) FY2022 Collaborative Researcher Grants (Y-22-03, and F-22-21).

Acknowledgments

XANES measurements were conducted with the approval of the Photon Factory, KEK, Tsukuba, Japan (Proposals No. 2021G076). We gratefully acknowledge Mitsunori Honda, Research Assistant Director, Japan Atomic Energy Agency for his help with XRD measurements.

Conflict of interest

The authors declare that the research was conducted in the absence of any commercial or financial relationships that could be construed as a potential conflict of interest.

Publisher's note

Supplementary material

The Supplementary Material for this article can be found online at: https://www.frontiersin.org/articles/10.3389/fnuen.2023.1142823/full#supplementary-material

References

Aharoni, C., and Sparks, D. L. (1991). Kinetics of soil chemical reactions. A theoretical treatment. *SSSA Spec. Publ. Soil. Sci. Soc. Am.*, 1–18. 1–18. doi:10.2136/sssaspecpub27.c1

Ahmad, M. A., Ahmad Puad, N. A., and Bello, O. S. (2014). Kinetic, equilibrium and thermodynamic studies of synthetic dye removal using pomegranate peel activated carbon prepared by microwave-induced KOH activation. *Water Resour. Ind.* 6, 18–35. doi:10.1016/j.wri.2014.06.002

Ahmad, M., Manzoor, K., Venkatachalam, P., and Ikram, S. (2016). Kinetic and thermodynamic evaluation of adsorption of Cu(II) by thiosemicarbazide chitosan. *Int. J. Biol. Macromol.* 92, 910–919. doi:10.1016/j.ijbiomac.2016.07.075

Alia, S. M., Jensen, K. O., Pivovar, B. S., and Yan, Y. (2012). Platinum-Coated palladium nanotubes as oxygen reduction reaction electrocatalysts. *ACS Catal.* 2, 858–863. doi:10.1021/cs200682c

Ayawei, N., Ebelegi, A. N., and Wankasi, D. (2017). Modelling and interpretation of adsorption isotherms. *J. Chem.*

Azcarate, I., Costentin, C., Methivier, C., Laberty-Robert, C., and Grimaud, A. (2018). Electron transfer at the metal oxide/electrolyte interface: A simple methodology for quantitative kinetics evaluation. *J. Phys. Chem. C* 122, 12761–12770. doi:10.1021/acs.jpcc.8b02289

Baek, M.-H., Ijagbemi, C. O., Se-Jin, O., and Kim, D.-S. (2010). Removal of Malachite Green from aqueous solution using degreased coffee bean. *J. Hazard. Mat.* 176, 820–828. doi:10.1016/j.jhazmat.2009.11.110

Beale, A. M., Paul, M., Sankar, G., Oldman, R. J., Catlow, C. R. A., French, S., et al. (2009). Combined experimental and computational modelling studies of the solubility of nickel in strontium titanate. *J. Mat. Chem.* 19, 4391–4400. doi:10.1039/b902591j

Boglaienko, D., Emerson, H. P., Katsenovich, Y. P., and Levitskaia, T. G. (2019). Comparative analysis of ZVI materials for reductive separation of 99Tc(VII) from aqueous waste streams. *J. Hazard. Mat.* 380, 120836. doi:10.1016/j.jhazmat.2019.120836

Buechele, A. C., Lukens, W. W., Shuh, D. K., McKeown, D. A., Muller, I. S., and Pegg, I. L. (2010). Comparison of the behavior of technetium and rhenium in low activity waste glass formulations subjected to the vapor hydration test. *Microsc. Microanal.* 16, 1628–1629. doi:10.1017/s143192761006232x

Burton-Pye, B. P., Radivojevic, I., McGregor, D., Mbomekalle, I. M., Lukens, W. W. J., and Francesconi, L. C. (2011). Photoreduction of 99Tc pertechnetate by nanometer-sized metal oxides: New strategies for formation and sequestration of low-valent technetium. *J. Am. Chem. Soc.* 133, 18802–18815. doi:10.1021/ja2060929

Byegård, J., Skålberg, M., Widestrand, H., and Tullborg, E.-L. (2001). Effects of heterogeneous porosity on retention–results from the TRUE laboratory experiments. *This*(2001), 203–210.

Chandra, S., Kumar, A., and Tomar, P. K. (2014). Synthesis of Ni nanoparticles and their characterizations. *J. Saudi Chem. Soc.* 18, 437–442. doi:10.1016/j.jscs.2011.09.008

Chung, Y.-S., Lee, B., Choo, K.-H., and Choi, S.-J. (2011). Removal of perrhenate anions in aqueous solutions using anion-exchange organic/inorganic hybrid nanoporous beads. *J. Ind. Eng. Chem.* 17, 114–119. doi:10.1016/j.jiec.2010.12.007

Cothern, C. R., and Lappenbusch, W. L. (1985). Regulatory development of the interim and revised regulations for radioactivity in drinking water-past and present issues and problems. *Heal. Phys.* 48, 535–551. doi:10.1097/00004032-198505000-00001

Cui, D., and Eriksen, T. E. (1996). Reduction of pertechnetate in solution by heterogeneous electron transfer from Fe(II)-Containing geological material. *Environ. Sci. Technol.* 30, 2263–2269. doi:10.1021/es950627v

Darab, J. G., Amonette, A. B., Burke, D. S. D., Orr, R. D., Ponder, S. M., Schrick, B., et al. (2007). Removal of pertechnetate from simulated nuclear waste streams using supported zerovalent iron. *Chem. Mat.* 19, 5703–5713. doi:10.1021/cm0607379

Ding, Q., Qian, T., Yang, F., Liu, H., Wang, L., Zhao, D., et al. (2013). Kinetics of reductive immobilization of rhenium in soil and groundwater using zero valent iron nanoparticles. *Environ. Eng. Sci.* 30, 713–718. doi:10.1089/ees.2012.0160

Dolor, M. K., Gilmour, C. C., and Helz, G. R. (2009). Distinct microbial behavior of Re compared to Tc: Evidence against microbial Re fixation in aquatic sediments. *Geomicrobiol. J.* 26, 470–483. doi:10.1080/01490450903060822

Eljamal, O., Eljamal, R., Maamoun, I., Khalil, A. M. E., Shubair, T., Falyouna, O., et al. (2022a). Efficient treatment of ammonia-nitrogen contaminated waters by nano zero-valent iron/zeolite composite. *Chemosphere* 287, 131990. doi:10.1016/j.chemosphere.2021.131990

Eljamal, O., Maamoun, I., Alkhudhayri, S., Eljamal, R., Falyouna, O., Tanaka, K., et al. (2022b). Insights into boron removal from water using Mg-Al-LDH: Reaction parameters optimization and 3D-RSM modeling. *J. Water Process Eng.* 46, 102608. doi:10.1016/j.jwpe.2022.102608

Eljamal, R., Eljamal, O., Maamoun, I., Yilmaz, G., and Sugihara, Y. (2020). Enhancing the characteristics and reactivity of nZVI: Polymers effect and mechanisms. *J. Mol. Liq.* 315, 113714. doi:10.1016/j.molliq.2020.113714

Emerson, H. P., Gebru, A., Boglaienko, D., Katsenovich, Y. P., Kandel, S., and Levitskaia, T. G. (2020). Impact of zero valent iron aging on reductive removal of technetium-99. *J. Environ. Chem. Eng.* 8, 103767. doi:10.1016/j.jece.2020.103767

Falyouna, O., Maamoun, I., Bensaida, K., Tahara, A., Sugihara, Y., and Eljamal, O. (2022). Encapsulation of iron nanoparticles with magnesium hydroxide shell for remarkable removal of ciprofloxacin from contaminated water. *J. Colloid Interface Sci.* 605, 813–827. doi:10.1016/j.jcis.2021.07.154

Fan, D., Anitori, R. P., Tebo, B. M., Tratnyek, P. G., Lezama Pacheco, J. S., Kukkadapu, R. K., et al. (2013). Reductive sequestration of pertechnetate (99TcO4–) by nano zerovalent iron (nZVI) transformed by abiotic sulfide. *Environ. Sci. Technol.* 47, 5302–5310. doi:10.1021/es304829z

Fu, L., Zu, J., He, L., Gu, E., and Wang, H. (2020). An adsorption study of 99Tc using nanoscale zero-valent iron supported on D001 resin. *Front. Energy* 14, 11–17. doi:10.1007/s11708-019-0634-y

Ghosal, P. S., and Gupta, A. K. (2015). An insight into thermodynamics of adsorptive removal of fluoride by calcined Ca–Al–(NO 3) layered double hydroxide. *RSC Adv.* 5, 105889–105900. doi:10.1039/c5ra20538g

Grillet, L., Ouerdane, L., Flis, P., Hoang, M. T. T., Isaure, M.-P., Lobinski, R., et al. (2014). Ascorbate efflux as a new strategy for iron reduction and transport in plants. *J. Biol. Chem.* 289, 2515–2525. doi:10.1074/jbc.m113.514828

Idham, M. F., Falyouna, O., Eljamal, R., Maamoun, I., and Eljamal, O. (2022). Chloramphenicol removal from water by various precursors to enhance graphene oxide–iron nanocomposites. *J. Water Process Eng.* 50, 103289. doi:10.1016/j.jwpe.2022.103289

Islam, M. S., Maamoun, I., Falyouna, O., Eljamal, O., and Saha, B. B. (2023). Arsenic removal from contaminated water utilizing novel green composite Chlorella vulgaris and nano zero-valent iron. *J. Mol. Liq.* 370, 121005. doi:10.1016/j.molliq.2022.121005

Jing, P., Liu, M., Pu, Y., Cui, Y., Wang, Z., Wang, J., et al. (2016). Dependence of phase configurations, microstructures and magnetic properties of iron-nickel (Fe-Ni) alloy nanoribbons on deoxidization temperature in hydrogen. *Sci. Rep.* 6, 37701–37709. doi:10.1038/srep37701

Karanjkar, P. U., Burt, S. P., Chen, X., Barnett, K. J., Ball, M. R., Kumbhalkar, M. D., et al. (2016). Effect of carbon supports on RhRe bifunctional catalysts for selective hydrogenolysis of tetrahydropyran-2-methanol. *Catal. Sci. Technol.* 6, 7841–7851. doi:10.1039/c6cy01763k

Kerli, S., and Soğuksu, A. K. (2019). Production of iron oxide and nickel oxide nanostructural particles, investigation of the supercapacitor and photocatalytic properties. *Z. für Krist. Mat.* 234, 725–731. doi:10.1515/zkri-2019-0043

Kim, D., and Kruger, A. A. (2018). Volatile species of technetium and rhenium during waste vitrification. *J. Non. Cryst. Solids* 481, 41–50. doi:10.1016/j.jnoncrysol.2017.10.013

Kim, H.-S., Ahn, J.-Y., Kim, C., Lee, S., and Hwang, I. (2014). Effect of anions and humic acid on the performance of nanoscale zero-valent iron particles coated with polyacrylic acid. *Chemosphere* 113, 93–100. doi:10.1016/j.chemosphere.2014.04.047

Komarneni, S., Li, Q. H., and Roy, R. (1996). Microwave-hydrothermal processing of layered anion exchangers. *J. Mat. Res.* 11, 1866–1869. doi:10.1557/jmr.1996.0236

Kumar, P. S., Ramalingam, S., Kirupha, S. D., Murugesan, A., Vidhyadevi, T., and Sivanesan, S. (2011). Adsorption behavior of nickel (II) onto cashew nut shell: Equilibrium, thermodynamics, kinetics, mechanism and process design. *Chem. Eng. J.* 167, 122–131. doi:10.1016/j.cej.2010.12.010

Lee, M.-S., Saslow, S. A., Um, W., Kim, D.-S., Kruger, A. A., Rousseau, R., et al. (2020). Impact of Cr and Co on 99Tc retention in magnetite: A combined study of *ab initio* molecular dynamics and experiments. *J. Hazard. Mat.* 387, 121721. doi:10.1016/j.jhazmat.2019.121721

Lee, M.-S., Um, W., Wang, G., Kruger, A. A., Lukens, W. W., Rousseau, R., et al. (2016). Impeding 99Tc (IV) mobility in novel waste forms. *Nat. Commun.* 7, 12067. doi:10.1038/ncomms12067

Lenell, B. A., and Arai, Y. (2017). Perrhenate sorption kinetics in zerovalent iron in high pH and nitrate media. *J. Hazard. Mat.* 321, 335–343. doi:10.1016/j.jhazmat.2016.09.024

Li, D., Seaman, J. C., Hunyadi Murph, S. E., Kaplan, D. I., Taylor-Pashow, K., Feng, R., et al. (2019). Porous iron material for TcO4- and ReO4- sequestration from groundwater under ambient oxic conditions. *J. Hazard. Mat.* 374, 177–185. doi:10.1016/j.jhazmat.2019.04.030

Li, J., Chen, C., Zhang, R., and Wang, X. (2016). Reductive immobilization of Re(VII) by graphene modified nanoscale zero-valent iron particles using a plasma technique. *Sci. China Chem.* 59, 150–158. doi:10.1007/s11426-015-5452-4

Liu, H., Qian, T., and Zhao, D. (2013). Reductive immobilization of perrhenate in soil and groundwater using starch-stabilized ZVI nanoparticles. *Chin. Sci. Bull.* 58, 275–281. doi:10.1007/s11434-012-5425-3

Liu, J., Hu, Q., Bi, W., Yang, L., Xiao, Y., Chow, P., et al. (2019). Altered chemistry of oxygen and iron under deep Earth conditions. *Nat. Commun.* 10, 153. doi:10.1038/s41467-018-08071-3

Liu, M., Feng, Z., Luan, X., Chu, W., Zhao, H., and Zhao, G. (2021). Accelerated Fe2+ regeneration in an effective electro-fenton process by boosting internal electron transfer to a nitrogen-conjugated Fe (III) complex. *Environ. Sci. Technol.* 55, 6042–6051. doi:10.1021/acs.est.0c08018

Liu, X., Wu, M., and Zhao, J. (2022). Removal of trichloroethylene from water by bimetallic Ni/Fe nanoparticles. *Water* 14, 1616. doi:10.3390/w14101616

Lovley, D. R. (1993). Dissimilatory metal reduction. *Annu. Rev. Microbiol.* 47, 263–290. doi:10.1146/annurev.mi.47.100193.001403

Lukens, W. W., McKeown, D. A., Buechele, A. C., Muller, I. S., Shuh, D. K., and Pegg, I. L. (2007). Dissimilar behavior of technetium and rhenium in borosilicate waste glass as determined by X-ray absorption spectroscopy. *Chem. Mater* 19, 559–566. doi:10.1021/cm0622001

Maamoun, I., Bensaida, K., Eljamal, R., Falyouna, O., Tanaka, K., Tosco, T., et al. (2022a). Rapid and efficient chromium (VI) removal from aqueous solutions using nickel hydroxide nanoplates (nNiHs). *J. Mol. Liq.* 358, 119216. doi:10.1016/j.molliq.2022.119216

Maamoun, I., Eljamal, O., Eljamal, R., Falyouna, O., and Sugihara, Y. (2020). Promoting aqueous and transport characteristics of highly reactive nanoscale zero valent iron via different layered hydroxide coatings. *Appl. Surf. Sci.* 506, 145018. doi:10.1016/j.apsusc.2019.145018

Maamoun, I., Eljamal, R., and Eljamal, O. (2023a). Statistical optimization of nZVI chemical synthesis approach towards P and NO3− removal from aqueous solutions: Cost-effectiveness and parametric effects. *Chemosphere* 312, 137176. doi:10.1016/j.chemosphere.2022.137176

Maamoun, I., Eljamal, R., Falyouna, O., Bensaida, K., Sugihara, Y., and Eljamal, O. (2021). Insights into kinetics, isotherms and thermodynamics of phosphorus sorption onto nanoscale zero-valent Iron. *J. Mol. Liq.* 328, 115402. doi:10.1016/j.molliq.2021.115402

Maamoun, I., Falyouna, O., Eljamal, R., Bensaida, K., Tanaka, K., Tosco, T., et al. (2022b). Multi-functional magnesium hydroxide coating for iron nanoparticles towards prolonged reactivity in Cr(VI) removal from aqueous solutions. *J. Environ. Chem. Eng.* 10, 107431. doi:10.1016/j.jece.2022.107431

Maamoun, I., Falyouna, O., Eljamal, R., Idham, M. F., Tanaka, K., and Eljamal, O. (2023b). Bench-scale injection of magnesium hydroxide encapsulated iron nanoparticles (nFe0@ Mg (OH) 2) into porous media for Cr (VI) removal from groundwater. *Chem. Eng. J.* 451, 138718. doi:10.1016/j.cej.2022.138718

Mardare, D., Yildiz, A., Apetrei, R., Rambu, P., Florea, D., Gheorghe, N. G., et al. (2012). The Meyer–Neldel rule in amorphous TiO2 films with different Fe content. *J. Mat. Res.* 27, 2271–2277. doi:10.1557/jmr.2012.193

Maset, E. R., Sidhu, S. H., Fisher, A., Heydon, A., Worsfold, P. J., Cartwright, A. J., et al. (2006). Effect of organic co-contaminants on technetium and rhenium speciation and solubility under reducing conditions. *Environ. Sci. Technol.* 40, 5472–5477. doi:10.1021/es061157f

Möllmann, A., Bialuschewski, D., Fischer, T., Tachibana, Y., Mathur, S., for E, O. B. T.-A. C., et al. (2020). "6 - functional metal oxide ceramics as electron transport medium in photovoltaics and photo-electrocatalysis," in *Elsevier series on advanced ceramic materials* (Elsevier), 207–273. doi:10.1016/B978-0-08-102726-4.00006-5

Mukherjee, R., Kumar, R., Sinha, A., Lama, Y., and Saha, A. K. (2016). A review on synthesis, characterization, and applications of nano zero valent iron (nZVI) for environmental remediation. *Crit. Rev. Environ. Sci. Technol.* 46, 443–466. doi:10.1080/10643389.2015.1103832

Nikolaychuk, P. A. (2022). The potential−−pH diagram for rhenium. *Chem. Thermodyn. Therm. Anal.* 7, 100068. doi:10.1016/j.ctta.2022.100068

Penke, Y. K., Anantharaman, G., Ramkumar, J., and Kar, K. K. (2019). Redox synergistic Mn-Al-Fe and Cu-Al-Fe ternary metal oxide nano adsorbents for arsenic remediation with environmentally stable As(0) formation. *J. Hazard. Mat.* 364, 519–530. doi:10.1016/j.jhazmat.2018.10.069

Powell, C. J., Jablonski, A., Naumkin, A., Kraut-Vass, A., Conny, J. M., and Rumble, J. R. (2001). NIST data resources for surface analysis by X-ray photoelectron spectroscopy and Auger electron spectroscopy. *J. Electron Spectros. Relat. Phenom.* 114 (116), 1097–1102. doi:10.1016/S0368-2048(00)00252-8

Qafoku, O., Pearce, C. I., Neumann, A., Kovarik, L., Zhu, M., Ilton, E. S., et al. (2017). Tc(VII) and Cr(VI) interaction with naturally reduced ferruginous smectite from a redox transition zone. *Environ. Sci. Technol.* 51, 9042–9052. doi:10.1021/acs.est.7b02191

Rivero-Huguet, M., and Marshall, W. D. (2009). Reduction of hexavalent chromium mediated by micro- and nano-sized mixed metallic particles. *J. Hazard. Mat.* 169, 1081–1087. doi:10.1016/j.jhazmat.2009.04.062

Rosser, T. E., Gross, M. A., Lai, Y.-H., and Reisner, E. (2016). Precious-metal free photoelectrochemical water splitting with immobilised molecular Ni and Fe redox catalysts. *Chem. Sci.* 7, 4024–4035. doi:10.1039/c5sc04863j

Saha, P., and Chowdhury, S. (2011). Insight into adsorption thermodynamics. *Thermodynamics* 16, 349–364.

Sahoo, Y., He, Y., Swihart, M. T., Wang, S., Luo, H., Furlani, E. P., et al. (2005). An aerosol-mediated magnetic colloid: Study of nickel nanoparticles. *J. Appl. Phys.* 98, 054308. doi:10.1063/1.2033145

Sakaguchi, A., Kadokura, A., Steier, P., Tanaka, K., Takahashi, Y., Chiga, H., et al. (2012). Isotopic determination of U, Pu and Cs in environmental waters following the fukushima daiichi nuclear power plant accident. *Geochem. J.* 46, 355–360. doi:10.2343/geochemj.2.0216

Saqalli, L., Galai, M., Gharda, N., Sahrane, M., Ghailane, R., Touhami, M. E., et al. (2018). Corrosion inhibition of carbon steel by anthraquinones derivatives in 1.0 M HCl: Electrochemical and quantum calculations. *Int. J. Electrochem Sci.* 13, 5096–5119. doi:10.20964/2018.05.40

Shagholani, H., Ghoreishi, S. M., and Mousazadeh, M. (2015). Improvement of interaction between PVA and chitosan via magnetite nanoparticles for drug delivery application. *Int. J. Biol. Macromol.* 78, 130–136. doi:10.1016/j.ijbiomac.2015.02.042

Sheng, G., Tang, Y., Linghu, W., Wang, L., Li, J., Li, H., et al. (2016). Enhanced immobilization of ReO4– by nanoscale zerovalent iron supported on layered double hydroxide via an advanced XAFS approach: Implications for TcO4– sequestration. *Appl. Catal. B Environ.* 192, 268–276. doi:10.1016/j.apcatb.2016.04.001

Shi, Z., Nurmi, J. T., and Tratnyek, P. G. (2011). Effects of nano zero-valent iron on oxidation– reduction potential. *Environ. Sci. Technol.* 45, 1586–1592. doi:10.1021/es103185t

Stallings, M. E., Barnes, M. J., Peters, T. B., Diprete, D. P., Hobbs, D. T., and Fink, S. D. (2005). *Characterization of supernate samples from high level waste tanks 13H, 30H, 37H, 39H, 45F, 46F and 49H*. Aiken, SC (United States): Savannah River Site.

Taguba, M. A. M., Ong, D. C., Ensano, B. M. B., Kan, C.-C., Grisdanurak, N., Yee, J.-J., et al. (2021). Nonlinear isotherm and kinetic modeling of Cu (II) and Pb (II) uptake from water by MnFe2O4/chitosan nanoadsorbents. *Water* 13, 1662. doi:10.3390/w13121662

Takahashi, Y., Uruga, T., Suzuki, K., Tanida, H., Terada, Y., and Hattori, K. H. (2007). An atomic level study of rhenium and radiogenic osmium in molybdenite. *Geochim. Cosmochim. Acta* 71, 5180–5190. doi:10.1016/j.gca.2007.08.007

Tanaka, K., Kozai, N., Ohnuki, T., and Grambow, B. (2019a). Study on coordination structure of Re adsorbed on Mg–Al layered double hydroxide using X-ray absorption fine structure. *J. Porous Mat.* 26, 505–511. doi:10.1007/s10934-018-0634-z

Tanaka, K., Kozai, N., Yamasaki, S., Ohnuki, T., Kaplan, D. I., and Grambow, B. (2019b). Adsorption mechanism of ReO4– on Ni–Zn layered hydroxide salt and its application to removal of ReO4– as a surrogate of TcO4. *Appl. Clay Sci.* 182, 105282. doi:10.1016/j.clay.2019.105282

Tanaka, K., Takahashi, Y., Sakaguchi, A. Y. A., Umeo, M., Hayakawa, S., Tanida, H., et al. (2012). Vertical profiles of iodine-131 and cesium-137 in soils in fukushima prefecture related to the fukushima daiichi nuclear power station accident. *Geochem. J.* 46, 73–76. doi:10.2343/geochemj.1.0137

Tang, J., Sun, Y., Zhang, C., Wang, L., Zhou, Y., Fang, D., et al. (2020). Reaction mechanism and process control of hydrogen reduction of ammonium perrhenate. *Met. (Basel)* 10, 640. doi:10.3390/met10050640

Tirez, K., Silversmit, G., Vincze, L., Servaes, K., Vanhoof, C., Mertens, M., et al. (2011). Speciation and fractionation of nickel in airborne particulate matter: Comparison between selective leaching and XAS spectroscopy. *J. Anal. At. Spectrom.* 26, 517–527. doi:10.1039/c0ja00049c

Tosco, T., Papini, M. P., Viggi, C. C., and Sethi, R. (2014). Nanoscale zerovalent iron particles for groundwater remediation: A review. *J. Clean. Prod.* 77, 10–21. doi:10.1016/j.jclepro.2013.12.026

Tougerti, A., Cristol, S., Berrier, E., Briois, V., La Fontaine, C., Villain, F., et al. (2012). XANES study of rhenium oxide compounds at theL1andL3absorption edges. *Phys. Rev. B* 85, 125136. doi:10.1103/PhysRevB.85.125136

Tran, H. N., You, S.-J., and Chao, H.-P. (2016). Thermodynamic parameters of cadmium adsorption onto orange peel calculated from various methods: A comparison study. *J. Environ. Chem. Eng.* 4, 2671–2682. doi:10.1016/j.jece.2016.05.009

Türk, M. (2014). *Particle Formation with supercritical fluids (supercritical fluid science and technology)*. Elsevier.

Vandergraaf, T. T., Drew, D. J., Archambault, D., and Ticknor, K. V. (1997). Transport of radionuclides in natural fractures: Some aspects of laboratory migration experiments. *J. Contam. Hydrol.* 26, 83–95. doi:10.1016/S0169-7722(96)00060-5

Venkateshaiah, A., Silvestri, D., Wacławek, S., Ramakrishnan, R. K., Krawczyk, K., Saravanan, P., et al. (2022). A comparative study of the degradation efficiency of chlorinated organic compounds by bimetallic zero-valent iron nanoparticles. *Environ. Sci. Water Res. Technol.* 8, 162–172. doi:10.1039/d1ew00791b

Wei, Y.-T., Wu, S.-C., Chou, C.-M., Che, C.-H., Tsai, S.-M., and Lien, H.-L. (2010). Influence of nanoscale zero-valent iron on geochemical properties of groundwater and vinyl chloride degradation: A field case study. *Water Res.* 44, 131–140. doi:10.1016/j.watres.2009.09.012

Wu, C., Tu, J., Liu, W., Zhang, J., Chu, S., Lu, G., et al. (2017). The double influence mechanism of pH on arsenic removal by nano zero valent iron: Electrostatic interactions and the corrosion of Fe0. *Environ. Sci. Nano* 4, 1544–1552. doi:10.1039/C7EN00240H

Wu, F. C., Tseng, R. L., and Juang, R. S. (2009). Initial behavior of intraparticle diffusion model used in the description of adsorption kinetics. *Chem. Eng. J.* 153, 1–8. doi:10.1016/j.cej.2009.04.042

Wu, T., Wang, H., Zheng, Q., Zhao, Y. L., and Li, J. Y. (2014). Effect of EDTA on the diffusion behavior of 99TcO4– and ReO4– in GMZ bentonite. *J. Radioanal. Nucl. Chem.* 299, 2037–2041. doi:10.1007/s10967-013-2831-1

Yan, L., Bing, J., and Wu, H. (2019). The behavior of ozone on different iron oxides surface sites in water. *Sci. Rep.* 9, 14752. doi:10.1038/s41598-019-50910-w

Yang, D., Guo, J., Lu, C., Song, Y., Li, H., Chen, Z., et al. (2018). A quasi-homogeneous catalysis and electron transfer chain for biodecolorization of azo dye by immobilized phenazine redox mediator. *Int. Biodeterior. Biodegrad.* 126, 69–77. doi:10.1016/j.ibiod.2017.09.018

Yang, G. C. C., Hung, C.-H., and Tu, H.-C. (2008). Electrokinetically enhanced removal and degradation of nitrate in the subsurface using nanosized Pd/Fe slurry. *J. Environ. Sci. Heal. Part A* 43, 945–951. doi:10.1080/10934520801974517

Yung, T.-Y., Huang, L.-Y., Chan, T.-Y., Wang, K.-S., Liu, T.-Y., Chen, P.-T., et al. (2014). Synthesis and characterizations of Ni-NiO nanoparticles on PDDA-modified graphene for oxygen reduction reaction. *Nanoscale Res. Lett.* 9, 444–446. doi:10.1186/1556-276x-9-444

Zachara, J. M., Heald, S. M., Jeon, B.-H., Kukkadapu, R. K., Liu, C., McKinley, J. P., et al. (2007). Reduction of pertechnetate [Tc(VII)] by aqueous Fe(II) and the nature of solid phase redox products. *Geochim. Cosmochim. Acta* 71, 2137–2157. doi:10.1016/j.gca.2006.10.025

Zhang, B., and Wang, D. (2019). Preparation of biomass activated carbon supported nanoscale zero-valent iron (nZVI) and its application in decolorization of methyl orange from aqueous solution. *Water* 11, 1671. doi:10.3390/w11081671

Zhang, Z., Hu, S., Baig, S. A., Tang, J., and Xu, X. (2012). Catalytic dechlorination of Aroclor 1242 by Ni/Fe bimetallic nanoparticles. *J. Colloid Interface Sci.* 385, 160–165. doi:10.1016/j.jcis.2012.07.024

Zhang, Z., Shen, Q., Cissoko, N., Wo, J., and Xu, X. (2010). Catalytic dechlorination of 2,4-dichlorophenol by Pd/Fe bimetallic nanoparticles in the presence of humic acid. *J. Hazard. Mat.* 182, 252–258. doi:10.1016/j.jhazmat.2010.06.022